OPEN ACCESS



SN 2020jgb: A Peculiar Type Ia Supernova Triggered by a Helium-shell Detonation in a Star-forming Galaxy

Chang Liu (刘畅)^{1,2}, Adam A. Miller^{1,2}, Abigail Polin^{3,4}, Anya E. Nugent^{1,2}, Kishalay De^{5,21}, Peter E. Nugent^{6,7}, Steve Schulze⁸, Avishay Gal-Yam⁹, Christoffer Fremling^{10,11}, Shreya Anand¹², Igor Andreoni^{13,14,15,22}, Peter Blanchard², Thomas G. Brink⁶, Suhail Dhawan¹⁶, Alexei V. Filippenko⁶, Kate Maguire¹⁷, Tassilo Schweyer¹⁸, Huei Sears^{1,2}, Yashvi Sharma¹¹, Matthew J. Graham¹¹, Steven L. Groom¹⁹, David Hale¹⁰, Mansi M. Kasliwal¹¹, Frank J. Masci¹⁹, Josiah Purdum¹⁰, Benjamin Racine²⁰, Jesper Sollerman¹⁸, and Shrinivas R. Kulkarni¹¹ Department of Physics and Astronomy, Northwestern University, 2145 Sheridan Road, Evanston, IL 60208, USA; ptg.cliu@u.northwestern.edu ² Center for Interdisciplinary Exploration and Research in Astrophysics (CIERA), Northwestern University, 1800 Sherman Ave, Evanston, IL 60201, USA The Observatories of the Carnegie Institution for Science, 813 Santa Barbara Street, Pasadena, CA 91101, USA ⁴ TAPIR, Walter Burke Institute for Theoretical Physics, 350-17, Caltech, Pasadena, CA 91125, USA ⁵ MIT-Kavli Institute for Astrophysics and Space Research, 77 Massachusetts Avenue, Cambridge, MA 02139, USA Department of Astronomy, University of California, Berkeley, CA 94720-3411, USA ⁷ Lawrence Berkeley National Laboratory, 1 Cyclotron Road, Berkeley, CA, 94720, USA ⁸ The Oskar Klein Centre, Department of Physics, Stockholm University, Albanova University Center, SE-106 91 Stockholm, Sweden Department of Particle Physics and Astrophysics, Weizmann Institute of Science, 76100 Rehovot, Israel ¹⁰ Caltech Optical Observatories, California Institute of Technology, Pasadena, CA 91125, USA Division of Physics, Mathematics, and Astronomy, California Institute of Technology, Pasadena, CA 91125, USA Cahill Center for Astrophysics, California Institute of Technology, Pasadena CA 91125, USA Joint Space-Science Institute, University of Maryland, College Park, MD 20742, USA
 Department of Astronomy, University of Maryland, College Park, MD 20742, USA ¹⁵ Astrophysics Science Division, NASA Goddard Space Flight Center, Mail Code 661, Greenbelt, MD 20771, USA 16 Institute of Astronomy and Kavli Institute for Cosmology, University of Cambridge, Madingley Road, Cambridge CB3 0HA, UK School of Physics, Trinity College Dublin, The University of Dublin, Dublin 2, Ireland ¹⁸ The Oskar Klein Centre, Department of Astronomy, Stockholm University, AlbaNova, SE-106 91 Stockholm, Sweden IPAC, California Institute of Technology, 1200 E. California Boulevard, Pasadena, CA 91125, USA ²⁰ Aix Marseille Univ, CNRS/IN2P3, CPPM, Marseille, France Received 2022 September 8; revised 2023 January 30; accepted 2023 February 10; published 2023 April 3

Abstract

The detonation of a thin ($\lesssim 0.03\,M_\odot$) helium shell (He-shell) atop a $\sim 1\,M_\odot$ white dwarf (WD) is a promising mechanism to explain normal Type Ia supernovae (SNe Ia), while thicker He-shells and less massive WDs may explain some recently observed peculiar SNe Ia. We present observations of SN 2020jgb, a peculiar SN Ia discovered by the Zwicky Transient Facility (ZTF). Near maximum brightness, SN 2020jgb is slightly subluminous (ZTF g-band absolute magnitude $-18.7\,\mathrm{mag} \lesssim M_g \lesssim -18.2\,\mathrm{mag}$ depending on the amount of host-galaxy extinction) and shows an unusually red color (0.2 mag $\lesssim g_{\mathrm{ZTF}} - r_{\mathrm{ZTF}} \lesssim 0.4\,\mathrm{mag}$) due to strong line-blanketing blueward of $\sim 5000\,\mathrm{\mathring{A}}$. These properties resemble those of SN 2018byg, a peculiar SN Ia consistent with an He-shell double detonation (DDet) SN. Using detailed radiative transfer models, we show that the optical spectroscopic and photometric evolution of SN 2020jgb is broadly consistent with a $\sim 0.95-1.00\,M_\odot$ (C/O core + He-shell) progenitor ignited by a $\gtrsim 0.1\,M_\odot$ He-shell. However, one-dimensional radiative transfer models without non-local-thermodynamic-equilibrium treatment cannot accurately characterize the line-blanketing features, making the actual shell mass uncertain. We detect a prominent absorption feature at $\sim 1\,\mu\mathrm{m}$ in the near-infrared (NIR) spectrum of SN 2020jgb, which might originate from unburnt helium in the outermost ejecta. While the sample size is limited, we find similar 1 $\mu\mathrm{m}$ features in all the peculiar He-shell DDet candidates with NIR spectra obtained to date. SN 2020jgb is also the first peculiar He-shell DDet SN discovered in a star-forming dwarf galaxy, indisputably showing that He-shell DDet SNe occur in both star-forming and passive galaxies, consistent with the normal SN Ia population.

Unified Astronomy Thesaurus concepts: Supernovae (1668); Type Ia supernovae (1728); White dwarf stars (1799); Observational astronomy (1145); Surveys (1671)

1. Introduction

It has been clear for decades that Type Ia supernovae (SNe Ia) are caused by the thermonuclear explosions of

Original content from this work may be used under the terms of the Creative Commons Attribution 4.0 licence. Any further distribution of this work must maintain attribution to the author(s) and the title of the work, journal citation and DOI.

carbon–oxygen (C/O) white dwarfs (WDs) in binary systems (see Maoz et al. 2014, for a review). Nevertheless, the nature of the binary companion, as well as how it ignites the WD, remains highly uncertain.

The helium-shell (He-shell) double detonation (DDet) scenario is one of the most promising channels to produce SNe Ia. In this scenario, the WD accretes from a companion to develop a helium-rich shell, which, after becoming sufficiently massive, could detonate. Such a detonation sends a shock wave into the C/O core to trigger a runaway thermonuclear explosion that inevitably disrupts and destroys the entire WD

NASA Einstein Fellow.

Neil Gehrels Fellow.

(Nomoto 1982a, 1982b; Woosley et al. 1986; Livne 1990; Woosley & Weaver 1994; Livne & Arnett 1995). This DDet mechanism can produce explosions of WDs below the Chandrasekhar-mass ($M_{\rm Ch}$).

There are several observational benchmarks for He-shell DDet SNe. Shortly after the ignition of the He-shell, the decay of radioactive material in the helium ashes may power a detectable flash (Woosley & Weaver 1994; Fink et al. 2010; Kromer et al. 2010). The Fe-group elements in the ashes will blanket blue photons with wavelengths $\lesssim 5000 \, \text{Å}$ (Kromer et al. 2010), the duration of which depends on the mass of the Heshell. For shells that are sufficiently thick, Boyle et al. (2017) suggest that the unburnt helium could provide an observational signal in near-infrared (NIR) spectra, and for those with a low progenitor mass ($\lesssim 1.0 \, M_{\odot}$), Polin et al. (2021) predict significant [Ca II] emission in the nebular phase of the SNe.

The He-shell DDet scenario could naturally account for the observational diversity in the SN Ia population. Using different sets of He-shell mass and C/O core mass, one can reproduce a variety of observables in "normal" SNe Ia with typical luminosities and spectral features near maximum brightness (e.g., Townsley et al. 2019; Magee et al. 2021; Shen et al. 2021), or peculiar subluminous ones (e.g., Polin et al. 2019).

For the He-shell DDet SNe that show "normal" characteristics near peak brightness, the mass of the C/O core should be $\gtrsim 1\,M_\odot$, and the mass of the He-shell is expected to be low ($\lesssim 0.03\,M_\odot$; Polin et al. 2019; Magee et al. 2021; Shen et al. 2021). Recently, it was reported that SN 2018aoz (Ni et al. 2022), an SN Ia showing a rapid redward color evolution within ~ 12 hr after first light, could be explained by a sub- $M_{\rm Ch}$ DDet model (a $1.05\,M_\odot$ C/O core and a $0.01\,M_\odot$ He-shell). After this red excess, the photometric evolution is consistent with that of normal SNe Ia, when the ashes of the He-shell become optically thin. However, some of its properties at maximum light and in the nebular phase are not consistent with an He-shell DDet scenario (Ni et al. 2023), making its nature debatable.

To date, only a small fraction of SNe Ia have been discovered sufficiently early for possible detection of a flux excess (e.g., Deckers et al. 2022), which has been identified in a handful of SNe Ia such as SN 2012cg (Marion et al. 2016), iPTF14atg (Cao et al. 2015), SN 2016jhr (Jiang et al. 2017), SN 2017cbv (Hosseinzadeh et al. 2017), SN 2018oh (Dimitriadis et al. 2019), SN 2019yvq (Miller et al. 2020), SN 2020hvf (Jiang et al. 2021), and SN 2021aefx (Ashall et al. 2022; Hosseinzadeh et al. 2022). While there could be a large underlying population of normal SNe Ia triggered by Heshell DDet, currently it is hard to verify this scenario.

In contrast, if the He-shell is sufficiently massive, such that the ashes of the shell remain optically thick over a much more extended time, the SN could appear unusually red even near maximum light. Such peculiar SNe Ia could be normal in brightness: SN 2016jhr is the only reported event that shows a normal peak luminosity ($M_B \approx -18.8$ mag), but it exhibits an early red flash and maintains a red g-r color throughout its evolution (Jiang et al. 2017). Its photometric evolution as well as its spectrum around maximum could be explained by a near- $M_{\rm Ch}$ DDet model. WD explosions with a total progenitor mass $<1\,M_\odot$ are expected to be subluminous. SN 2018byg (De et al. 2019) is a prototype of this subclass. Other candidates include OGLE-2013-SN-079 (Inserra et al. 2015), SN 2016dsg (Dong et al. 2022a), SN 2016hnk (Jacobson-Galán et al. 2020; see, Galbany et al. 2019), and SN 2019ofm (De et al. 2020).

These events are faint, red, and show strong line-blanketing in spectra at maximum light. A tentative detection of unburnt helium in SN 2016dsg was also reported by Dong et al. (2022a). We refer to these events as peculiar He-shell DDet SNe.²³ The small sample size to date suggests this SN Ia subclass might be intrinsically rare.

In this paper, we present observations of another peculiar He-shell DDet event, SN 2020jgb. This peculiar SN Ia highly resembles SN 2018byg in photometric and spectroscopic properties, and exhibits a remarkable feature in the NIR spectrum that could be attributed to unburnt helium. In Section 2, we report the observations of SN 2020jgb, which are analyzed in Section 3, where we show its similarities with other He-shell DDet SNe and discuss the tentative He I absorption features. We use a grid of He-shell DDet models to fit the data of SN 2020jgb, and present the results in Section 4.1. Then we expand our discussion to other He-shell DDet SNe, discussing the possibly ubiquitous absorption features in their NIR spectra near 1 μ m (Section 4.2) and their diversity in host environments (Section 4.3). We draw our conclusions in Section 5.

Along with this paper, we have released the data utilized in this study and the software used for data analysis and visualization. They are available online at https://github.com/slowdivePTG/SN2020jgb.

2. Observations

2.1. Discovery

SN 2020jgb was first discovered by the Zwicky Transient Facility (ZTF; Bellm et al. 2019a; Graham et al. 2019; Dekany et al. 2020) on 2020 May 03.463 (UT dates are used throughout this paper; MJD 58972.463) with the 48 inch Samuel Oschin Telescope (P48) at Palomar Observatory. The automated ZTF discovery pipeline (Masci et al. 2019) detected SN 2020jgb using the imagedifferencing technique of Zackay et al. (2016). The candidate passed internal thresholds (e.g., Duev et al. 2019; Mahabal et al. 2019), leading to the production and dissemination of a real-time alert (Patterson et al. 2019) and the internal designation ZTF20aayhacx. It was detected with $g_{\rm ZTF} = 19.86 \pm 0.15$ mag at $\alpha_{\rm J2000} = 17^{\rm h}53^{\rm m}12^{\rm s}.651$, $\delta_{\rm J2000} = -00^{\circ}51'21''.81$ and announced to the public by Fremling (2020). The host galaxy, PSO J175312.663+005122.078, is a dwarf galaxy, to which SN 2020jgb has a projected offset of only 0.73. The last nondetection limits the brightness to $r_{\text{ZTF}} > 20.7$ mag on 2020 April 27.477 (MJD 58966.477; 5.99 days before the first detection). This transient was classified as an SN Ia by Dahiwale & Fremling (2020). We confirm this classification via SuperNova IDentification (SNID; Blondin & Tonry 2007), which shows SN 2020jgb is most consistent with SNe Ia. Templates of other hydrogen-poor SNe, including Type Ib and Type Ic SNe, do not match the spectral sequence of SN 2020jgb.

2.2. Host-galaxy Observations

On 2022 March 31, two years after the transient faded, we took a spectrum of its host galaxy using the DEep Imaging Multi-Object Spectrograph (DEIMOS; Faber et al. 2003) on the Keck II 10 m

 $[\]overline{^{23}}$ In the literature they are also referred to as thick He-shell DDet SNe, which describes the physics leading to their peculiar evolution. This definition is imprecise, however, because the threshold for an He-shell to be "thick" depends on core mass; low-mass WDs (\lesssim 0.8 M_{\odot}) with low-mass He-shells (\lesssim 0.03 M_{\odot}) can still produce red, subluminous events (e.g., Shen et al. 2021).

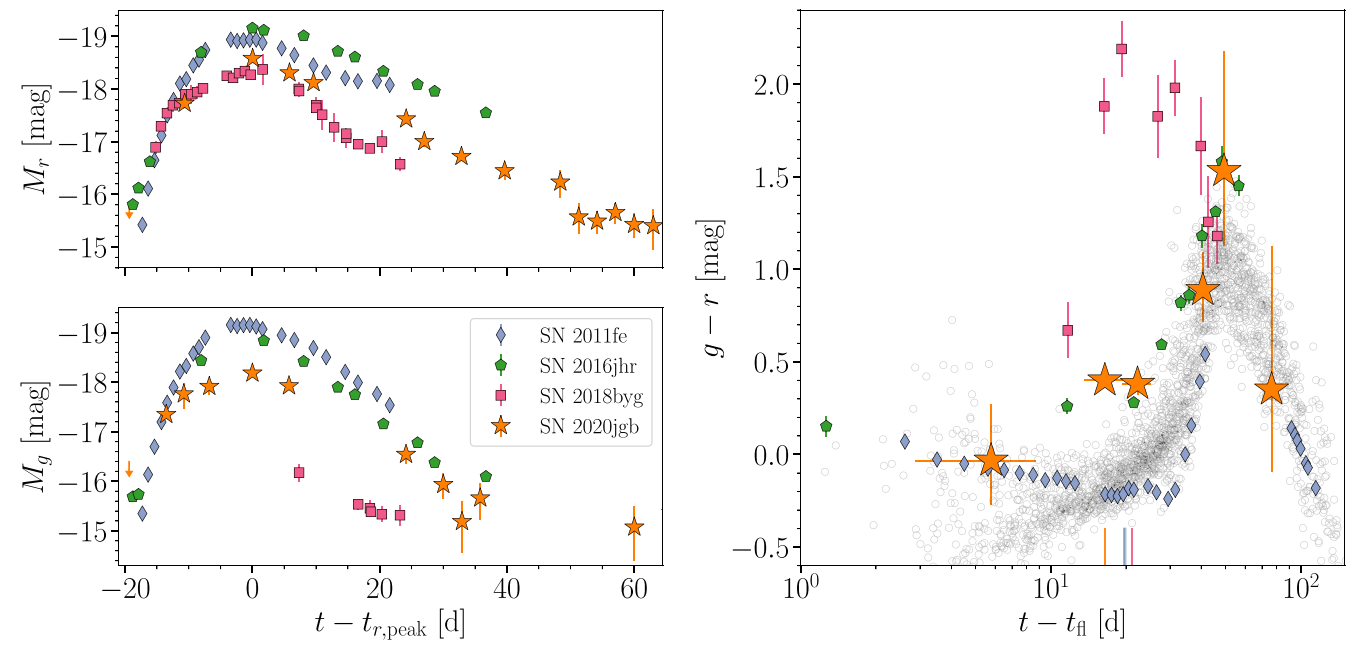


Figure 1. Comparison of the photometric properties of SN 2020jgb with those of SN 2011fe (normal SN Ia; Pereira et al. 2013), SN 2016jhr (normal-luminosity Heshell DDet; Jiang et al. 2017), and SN 2018byg (subluminous He-shell DDet; De et al. 2019). Left: multiband light curves. The upper (lower) panel shows the evolution in the *r*-band (*g*-band) absolute magnitude. The arrows mark the 5σ limit of the last nondetections of SN 2020jgb in g_{ZTF} and r_{ZTF} . Right: g - r color evolution. For each object, the peak epoch is marked by a vertical line with the corresponding color on the bottom axis. The gray circles denote the $g_{ZTF} - r_{ZTF}$ color evolution of 62 normal SNe Ia (open circles) with prompt observations within 5 days of first light by ZTF (Bulla et al. 2020).

telescope, with a total integration time of 3200 s. It was reduced with the PypeIt Python package (Prochaska et al. 2020). The host exhibits strong, narrow emission lines including $H\alpha$, $H\beta$, [N II] $\lambda\lambda$ 6548, 6583, [O III] $\lambda\lambda$ 4959, 5007, and [S II] $\lambda\lambda$ 6716, 6731. By fitting all these emission features with Gaussian profiles, we obtain an average redshift of $z=0.0307\pm0.0003$. With the diagnostic emission-line equivalent width (EW) ratios (log([N II]/ $H\alpha$) = -1.05 ± 0.08 and log([O III]/ $H\beta$) = 0.19 ± 0.02), ²⁴ the host is consistent with star-forming galaxies in the Baldwin et al. (1981, hereafter BPT) diagram (see also Veilleux & Osterbrock 1987). Additional discussion of the host galaxy's properties is presented in Section 4.3.

To estimate the distance modulus of SN 2020jgb, we first use the 2M++ model (Carrick et al. 2015) to estimate the peculiar velocity of its host galaxy, PSO J175312.663+005122.078, to be $179 \pm 250 \, \mathrm{km \, s^{-1}}$. This, combined with the recession velocity in the frame of the cosmic microwave background²⁵ (CMB) $v_{\mathrm{CMB}} = 9136 \, \mathrm{km \, s^{-1}}$, yields a net Hubble recession velocity of $9307 \pm 250 \, \mathrm{km \, s^{-1}}$. Adopting $H_0 = 70 \, \mathrm{km \, s^{-1} \, Mpc^{-1}}$, $\Omega_M = 0.3$, and $\Omega_{\Lambda} = 0.7$, we estimate the luminosity distance of SN 2020jgb to be 136.1 Mpc, equivalent to a distance modulus of $\mu = 35.67 \pm 0.06 \, \mathrm{mag}$.

To evaluate the potential host-galaxy extinction, we measure the Balmer decrement and find the flux ratio of $H\alpha$ to $H\beta$ to be 3.26 ± 0.13 , while the theoretical, extinction-free value is 2.86 (assuming case B recombination; Osterbrock & Ferland 2006). Using the extinction law from Fitzpatrick (1999) and assuming $R_V = 3.1$, this yields $E(B - V) = 0.11 \pm 0.04$ mag. This result is consistent with a model of the host galaxy's spectral energy distribution (SED; illustrated in Section 4.3), $E(B - V) = 0.13 \pm 0.01$ mag. As we do not

know the precise location of SN 2020jgb within its host galaxy, we adopt these reddening values as an upper limit to the total host-galaxy reddening.

2.3. Optical Photometry

SN 2020jgb was monitored in the $g_{\rm ZTF}$ and $r_{\rm ZTF}$ bands by ZTF as part of its ongoing Northern Sky Survey (Bellm et al. 2019b). We adopt a Galactic extinction of $E(B-V)_{\rm MW}=0.404$ mag (Schlafly & Finkbeiner 2011), and correct all photometry using the Fitzpatrick (1999) extinction model. The host extinction is not well constrained. While the potential host extinction could be up to $E(B-V)_{\rm host}\approx 0.13$, the lack of Na I D absorption at the redshift of the host galaxy is consistent with no additional host extinction, though see Poznanski et al. (2011) for caveats on the use of Na I D absorption as a proxy for extinction. Thus throughout the paper, we adopt a fiducial assumption of no host extinction and discuss the possible effects of addition extinction on constraining the progenitor properties in Section 4.1. Unless otherwise specified, the data displayed in the figures are only corrected for Galactic extinction

The forced-photometry absolute light curves²⁶ in $g_{\rm ZTF}$ and $r_{\rm ZTF}$ are shown in Figure 1, where we display all measurements having a signal-to-noise ratio (S/N) greater than 2. The light curves are reduced using the pipeline from A. A. Miller et al. (2023, in preparation); see also Yao et al. (2019).

2.4. Optical Spectroscopy

We obtained optical spectra of the object from \sim -10 to \sim +150 days relative to the $r_{\rm ZTF}$ -band peak, 27 using the

 $^{^{\}overline{24}}$ Here [N II] denotes the EW of the [N II] $\lambda6583$ line, and [O III] denotes the EW of the [O III] $\lambda5007$ line.

https://ned.ipac.caltech.edu/velocity_calculator

https://web.ipac.caltech.edu/staff/fmasci/ztf/forcedphot.pdf

 $^{^{27}}$ Unless otherwise specified, the "peak" or "maximum brightness" of SN 2020jgb refers to its maximum $r_{\rm ZTF}$ -band brightness.

 Table 1

 Spectroscopic Observations of SN 2020jgb and the Host Galaxy

t _{obs} (MJD)	Phase (days)	Telescope/ Instrument	$R \\ (\lambda/\Delta\lambda)$	Range (Å)	Airmass
58,976.42	-9.7	P60/SEDM	100	3770–9220	1.23
58,982.12	-4.2	NOT/	360	4000-9620	1.17
		ALFOSC			
58,990.43	+3.9	P60/SEDM	100	3770-9220	1.23
58,997.44	+10.7	P60/SEDM	100	3770-9220	1.29
58,998.41	+11.6	Shane/Kast	750	3620-10720	1.28
59,008.41	+21.3	P60/SEDM	100	3770-9220	1.28
59,009.45	+22.4	Gemini-N/	1800	8230-25150	1.07
		GNIRS			
59,010.40	+23.3	P200/DBSP	700	3200-9500	1.27
59,023.58	+36.1	Keck I/LRIS	1100	3200-10250	2.04
59,107.29	+117.3	Keck I/LRIS	1100	3200-10250	1.31
59,143.26	+152.2	Keck I/LRIS	1100	3200-10250	2.16
59,669.60	host	Keck II/ DEIMOS	2100	4500-8700	1.14

Note. Phase is measured relative to the r_{ZTF} -band peak in the rest frame of the host galaxy. The resolution R is reported for the central region of the spectrum.

Spectral Energy Distribution Machine (SEDM; Blagorodnova et al. 2018) on the automated 60 inch telescope (P60; Cenko et al. 2006) at Palomar Observatory, the Kast Double Spectrograph (Miller & Stone 1994) on the Shane 3 m telescope at Lick Observatory, the Andalucia Faint Object Spectrograph and Camera (ALFOSC)²⁸ installed at the Nordic Optical Telescope (NOT), the Double Spectrograph (DBSP) on the 200 inch Hale telescope (P200; Oke & Gunn 1982), and the Low Resolution Imaging Spectrometer (LRIS) on the Keck I 10 m telescope (Oke et al. 1995). With the exception of observations obtained with SEDM, all spectra were reduced using standard procedures (e.g., Matheson et al. 2000). The SEDM spectra were reduced using the custom pysedm software package (Rigault et al. 2019). Details of the spectroscopic observations are listed in Table 1, and the resulting spectral sequence is shown in Figure 2. All the spectra listed in Table 1 will be available on WISeREP (Yaron & Gal-Yam 2012).

2.5. Near-Infrared Spectroscopy

We obtained one NIR (0.8–2.5 μ m) spectrum of SN 2020jgb using the Gemini near-infrared spectrometer (GNIRS; Elias et al. 1998) on the Gemini North telescope on 2020 June 9 (~22 days after $r_{\rm ZTF}$ -band peak), with a total integration time of 2400 s. The GNIRS spectrum was reduced with PypeIt.

3. Analysis

3.1. Photometric Properties

SN 2020jgb exhibited a fainter light curve than normal SNe Ia. In Figure 1, we compare the photometric properties of SN 2020jgb with the nearby, well-observed SN 2011fe in g_{ZTF} and r_{ZTF} synthetic photometry from the spectrophotometric time series of Pereira et al. (2013), as well as two peculiar He-shell DDet events —the normal-luminosity event SN 2016jhr (Jiang et al. 2017) and the subluminous event SN 2018byg (De et al. 2019). All of these light curves have been corrected for Galactic reddening, while K-

corrections have not been performed,²⁹ because we do not have complete spectral sequences of these peculiar events.

While the observational coverage is sparse in the rise to maximum light, from Figure 1 it is clear that SN 2020igb is less luminous than normal SNe Ia (e.g., SN 2011fe). If the host galaxy reddens SN 2020jgb by $E(B - V)_{host} = 0.13$ mag, then SN 2020jgb would be \sim 0.3 mag brighter in the $r_{\rm ZTF}$ band and \sim 0.5 mag in the $g_{\rm ZTF}$ band, making it comparable to SN 2011fe in $r_{\rm ZTF}$, yet still ~ 0.5 mag fainter in $g_{\rm ZTF}$. In the right panel of Figure 1, we compare the color evolution (g - r) of these objects relative to the measured time of first light $t_{\rm fl}$, accompanied by 62 normal SNe Ia (open circles) observed within 5 days of $t_{\rm fl}$ by ZTF (from Bulla et al. 2020). They have been corrected for Galactic extinction, but K-corrections have not been performed for consistency. For SN 2020jgb, the early rise of the light curve was not well sampled, so we estimate $t_{\rm fl}$ as the midpoint of the first detection and the last nondetection. We adopt an uncertainty in this estimate of 3 days. All three He-shell DDet candidates are undoubtedly redder than normal SNe Ia. At maximum light, SN 2020jgb $(g_{\rm ZTF} - r_{\rm ZTF} \approx 0.4$ mag) was not as red as SN 2018byg $(g - r \approx 2.2 \text{ mag})$, but exhibited a similar color to SN 2016jhr $(g - r \approx 0.3 \text{ mag})$. Adopting $E(B-V)_{host} = 0.13$ mag still results in a relatively red color for SN 2020jgb ($g_{\rm ZTF} - r_{\rm ZTF} \approx 0.2$ mag) compared to normal SNe Ia $(g_{\text{ZTF}} - r_{\text{ZTF}} \approx -0.1 \text{ mag}).$

Interestingly, for both SN 2018byg and SN 2020jgb, near their maximum light the spectra sharply peak at \sim 5200 Å in the SN rest frame (see Figure 2), which is close to the red edge of the $g/g_{\rm ZTF}$ filter (\sim 4000–5500 Å). Thus, modest redshifts ($z \gtrsim 0.03$) can produce significant K-corrections, which constitute a substantial fraction of the observed red g-r colors for these events. For SN 2020jgb, using the ALFOSC spectrum obtained at -4 days, we estimate the K-correction to be $K_{g-r} \approx -0.2$ mag, the g-r color being bluer in the rest frame. SN 2018byg is at a higher redshift (z=0.066) so the K-correction is more extreme ($K_{g-r} \approx -1.0$ mag). Future efforts to identify additional subluminous He-shell DDet candidates can utilize the red g-r color to improve their search efficiency.

3.2. Optical Spectral Properties

In Figure 2, we show the optical spectral sequence of SN 2020jgb, and compare its spectra with those of some other SNe Ia at similar phases relative to peak brightness. For the spectra obtained after +100 days there is clear contamination from the host galaxy, including the presence of narrow emission lines. For these spectra we subtract the galaxy light as measured in the DEIMOS spectrum from 2022 (see Section 2.4). The earliest spectrum was obtained by SEDM \sim 10 days before $r_{\rm ZTF}$ -band peak. We only show portions of the binned spectrum where S/N > 2.5. The continuum is almost featureless with some marginal detection of Si II $\lambda 6355$ at \sim 6100 Å, the hallmark of SNe Ia. The subsequent spectra show a strong suppression of flux blueward of $\sim 5000 \text{ Å}$, 30 one of the major differences from those of normal SNe Ia. The Si II features become more prominent and are clearly detected until ~12 days after maximum light. We measure Si II expansion velocities following a procedure similar to that of Childress et al. (2013, 2014) and Maguire et al. (2014). The fitting region

²⁸ http://www.not.iac.es/instruments/alfosc/

 $[\]overline{^{29}}$ These SNe were all observed in slightly different g and r filters.

 $^{^{30}}$ This feature is prominent in SN 2020jgb when we adopt $\it E(B-V)_{\rm host}=0.0$ or 0.13 mag.

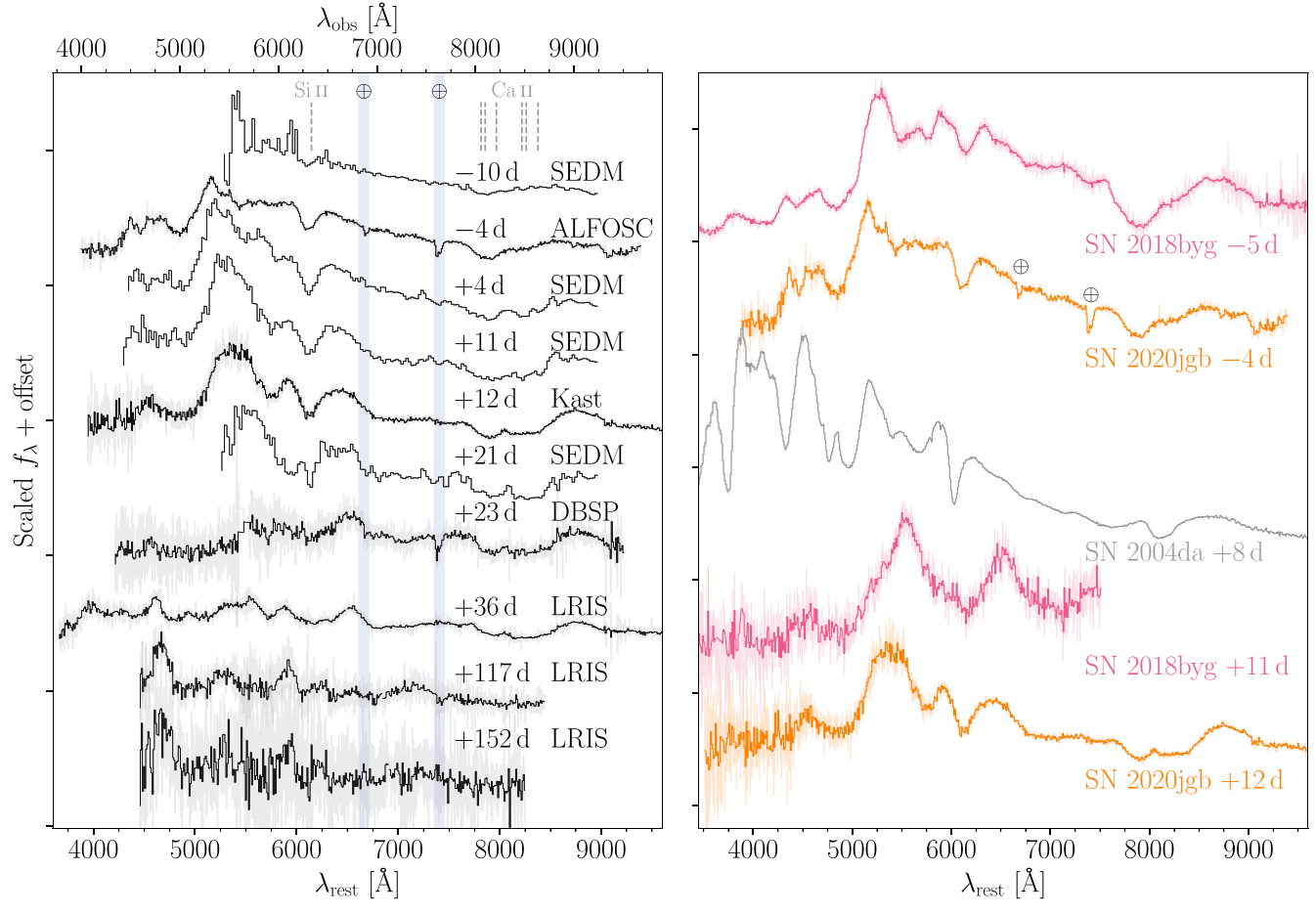


Figure 2. The optical spectral evolution of SN 2020jgb is typical of that of a peculiar SN Ia triggered by an He-shell DDet. Left: optical spectral sequence of SN 2020jgb. Rest-frame phases (days) relative to the r_{ZTF} -band peak and instruments used are posted next to each spectrum. Spectra have been corrected for $E(B-V)_{MW}=0.404$ mag and are shown in gray. The black lines are binned spectra with a bin size of 10 Å, except for the SEDM spectra, whose resolution is lower than the bin size. In the last two spectra, we have subtracted the light from the host galaxy. Only regions with S/N>2.5 after binning are plotted. The corresponding wavelengths of the Si II $\lambda 6355$ line (with an expansion velocity of $10,000 \, \mathrm{km \, s^{-1}}$) and the Ca II IRT (with expansion velocities of both $10,000 \, \mathrm{km \, s^{-1}}$ and $25,000 \, \mathrm{km \, s^{-1}}$) are marked by the vertical dashed lines. Right: spectral comparison with SN 2018byg (subluminous He-shell DDet; De et al. 2019) and SN 2004da (normal luminosity; Silverman et al. 2012).

is selected by visual inspection. The continuum is assumed to be linear, and the absorption profile after the continuum normalization is assumed to be composed of double Gaussian profiles centered at 6347 Å and 6371 Å. Within the model, the continuum flux densities at the blue and red edges are free parameters for which we adopt a normal distribution as a prior. The mean and standard deviation for the distribution are the observed flux density and its uncertainty (respectively) at each edge of the fitting region. Three more parameters (amplitude, mean velocity, logarithmic velocity dispersion) are used to characterize the double Gaussian profile, whose priors are set to be flat. This means the depths and widths of both peaks are forced to be the same, as Maguire et al. (2014) adopted in the optically thick regime. The posteriors of the five parameters are sampled simultaneously with emcee (Foreman-Mackey et al. 2013) using the Markov Chain Monte Carlo method. We find that the mean expansion velocity is $\sim 11,500 \,\mathrm{km \, s^{-1}}$ near maximum light.

In many SNe Ia, the Ca II near-infrared triplet (Ca II IRT) $\lambda\lambda$ 8498, 8542, 8662 causes two distinct components (Mazzali et al. 2005), which are conventionally referred to as photospheric-velocity features (PVFs) and high-velocity features (HVFs). The PVFs originate from the main line-forming region with typical photospheric (i.e., bulk ejecta) velocities, while the

HVFs are blueshifted to much shorter wavelengths, indicating significantly higher (by $\gtrsim 6000 \, \mathrm{km \, s^{-1}}$) velocities than typical PVFs (Silverman et al. 2015). Figure 2 shows that SN 2020jgb has prominent HVFs of Ca II IRT. The HVFs are visible in our first spectrum of SN 2020jgb at -10 days, and remain prominent through +36 days. Using the same technique we use to model the Si II features, we fit the HVFs and PVFs simultaneously. Both are fit by multiple Gaussian profiles assuming each line in the triplet can be approximated by the same profile (i.e., same amplitude and velocity dispersion). A best-fit expansion velocity of HVFs at $-10 \,\mathrm{days}$ is \sim 26,000 km s⁻¹. In the spectrum at -4 days, we observe a clear delineation between the HVFs and PVFs. For this and subsequent spectra, we fit the broad absorption features with two different velocity components simultaneously. From -4 to +23 days, the speed of the HVFs declines slightly to $\sim\!24,\!000\,\mathrm{km\,s}^{-1},$ and the speed of PVFs declines from \sim 11,000 to \sim 9000 km s⁻¹. As in normal SNe Ia, the relative strength between the HVFs and PVFs decreases with time. In Table 2 we report the evolution of the expansion velocity of Si II $\lambda 6355$ and the Ca II IRT.

We obtained two LRIS spectra at +117 days and +152 days, both of which are dominated by Fe-group elements and resemble those of normal SNe Ia (e.g., SN 2011fe; Mazzali et al. 2015),

Table 2 The Evolution of the Expansion Velocity of Si II $\lambda 6355$ and Ca II IRT and the Velocity of the 1 μ m Feature Assuming an He I Origin in the GNIRS Spectrum

Phase (days)	$(10^3 \mathrm{km}\mathrm{s}^{-1})$	$^{\nu_{\rm Ca~II,PVF}}$ $(10^3~{\rm km~s}^{-1})$	$v_{\text{Ca II,HVF}}$ (10^3 km s^{-1})	$^{\nu_{\text{He I?}}}$ (10^3km s^{-1})
-9.7		15.33 ± 0.12	25.88 ± 0.25	
-4.2	11.737 ± 0.073	11.18 ± 0.23	24.22 ± 0.11	
+3.9	11.356 ± 0.085	9.76 ± 0.21	24.17 ± 0.30	
+10.7	11.53 ± 0.20	8.8 ± 1.0	24.0 ± 1.1	
+11.6	11.239 ± 0.075	9.40 ± 0.13	24.58 ± 0.11	
+21.3	10.46 ± 0.21	9.10 ± 0.59	24.16 ± 0.69	
+22.4			•••	26.178 ± 0.062
+23.3		9.57 ± 0.46	23.59 ± 0.47	
+36.1	•••	9.57 ± 0.15	23.84 ± 0.15	•••

showing some enhancement in flux between ~4500 and \sim 6000 Å. There are no signs of emission due to the [Ca II] $\lambda\lambda$ 7291, 7324 doublet.

SN 2020jgb does not show any absorption features associated with O I λ 7774. While the low luminosity, red color, absence of hydrogen features, and star-forming host galaxy of SN 2020jgb are also reminiscent of Type Ic SNe (SNe Ic), which arise from stripped-envelope massive stars, SNe Ic usually exhibit stronger O I λ 7774 lines. The ratio of the relative line depths³¹ between the O_I λ 7774 line and the Si_{II} λ 6355 line is expected to be greater than 1 in typical SNe Ic (Gal-Yam 2017; Sun & Gal-Yam 2017). SN 2020jgb additionally does not show [O I] or [Ca II] emission lines in the nebular phase, which are ubiquitous in SNe Ic (Jerkstrand 2017). Consequently, we can definitively conclude SN 2020jgb is not an SN Ic.

The observational properties of SN 2020jgb are distinct from those of other subluminous thermonuclear SNe, including SN 2002cx-like (02cx-like; 32 Li et al. 2003), SN 1991bg-like (91bg-like; Filippenko et al. 1992), and SN 2002es-like (02eslike; Ganeshalingam et al. 2012) objects. The 02cx-like subclass is known to show a much bluer color near peak luminosity $(g - r \approx 0 \text{ mag}; \text{ Miller et al. } 2017)$ than SN 2020jgb. While 91bg-like and 02es-like SNe are redder than normal SNe Ia (due to the Ti II absorption trough at \sim 4200 Å), they exhibit significant emission blueward of \sim 5000 Å. They also do not exhibit HVFs of Ca II IRT (e.g., Silverman et al. 2015), in contrast to SN 2020jgb.

The optical spectral evolution of SN 2020jgb resembles that of SN 2018byg, a subluminous He-shell DDet SN. At early times, both SNe were relatively blue and featureless, with broad and shallow Ca II IRT absorption. As they evolved closer to maximum light, they developed strong continuous absorption blueward of \sim 5000 Å. Meanwhile, Si II λ 6355 and the Ca II IRT became more prominent. Neither O I nor S II was detected in either object. In the He-shell DDet scenario, a large amount of Fe-group elements would be synthesized in the shell, which would cause significant line-blanketing near maximum light (Kromer et al. 2010; Polin et al. 2019) and high-velocity intermediate-mass elements like Ca II (Fink et al. 2010; Kromer et al. 2010; Shen & Moore 2014). The similarity to SN 2018byg makes SN 2020jgb another promising He-shell DDet SN candidate.

3.3. NIR Spectral Properties

The NIR spectrum of SN 2020jgb is compared with those of a normal SNe Ia (SN 2004da; data from Marion et al. 2009) and two subluminous SNe Ia (SN 1999by and iPTF13ebh; Höflich et al. 2002; Hsiao et al. 2015) at a similar phase in Figure 3. SN 2020jgb shows a strong absorption feature at \sim 0.99 μ m, which is not seen in normal SNe Ia. This feature was still significant two weeks later, as detected with LRIS on Keck (see Figure 6), though it was only partially covered. Aside from this prominent feature, SN 2020jgb resembles normal SNe Ia in the NIR. The shape of the continuum redward of $\sim 1.2 \,\mu \text{m}$ is significantly altered by line-blanketing from Fe-group elements. Just like normal and other subluminous SNe Ia, SN 2020jgb shows an enhancement of flux at about 1.30, 1.55, 2.00, 2.10, and 2.25 μ m, accompanied by several Co II absorption lines. It is especially similar to SN 2004da at +25 days as the steep increase in flux at $\sim 1.55 \,\mu\text{m}$, known as the *H*-band break (Hsiao et al. 2019), has become less prominent. To summarize, the NIR spectrum of SN 2020jgb is dominated by Fe-group elements, consistent with the nucleosynthetic yield of a WD thermonuclear explosion. However, the 1 μ m feature adds to the peculiarities of SN 2020jgb as an SN Ia.

Marion et al. (2009) presented a sample of 15 NIR spectra of normal SNe Ia between +14 and +75 days relative to maximum light, and none of those spectra show prominent absorption features around 1 μ m. We have investigated several potential identifications for this feature (see below), none of which provides a completely satisfying explanation.

The most tantalizing possibility is that the absorption is due to He I λ 10830. Modern DDet models reveal that part of the helium in the shell will be left unburnt (e.g., Kromer et al. 2010; Woosley & Kasen 2011; Polin et al. 2019). With full non-local-thermodynamic-equilibrium (nLTE) physics taken into consideration, He I features are unambiguously expected in some He-shell DDet SNe, among which He I $\lambda 10830$ is the most prominent absorption line (Dessart & Hillier 2015; Boyle et al. 2017).³³ Figure 6 shows that the $1 \mu m$ feature, if associated with He I λ 10830, has a velocity of \sim 26,000 km s⁻ which stays roughly the same from \sim 22 to \sim 36 days after maximum light. This speed is consistent with the unburnt helium in He-shell DDet models when the ejecta have reached homologous expansion (Kromer et al. 2010; Polin et al. 2019), yet it is unclear whether the high-velocity unburnt helium could

 $[\]overline{^{31}}$ The relative depth is defined as the absorption line depth relative to the pseudo-continuum. See Sun & Gal-Yam (2017) for more details.

32 This subclass is also referred to as Type Iax SNe (Foley et al. 2013).

³³ Since helium has high excitation states, optical and NIR helium lines require nonthermal excitation (e.g., collision with fast electrons; Lucy 1991). Models assuming LTE radiative transfer neglect nonthermal effects; thus, they are not able to characterize the helium features.

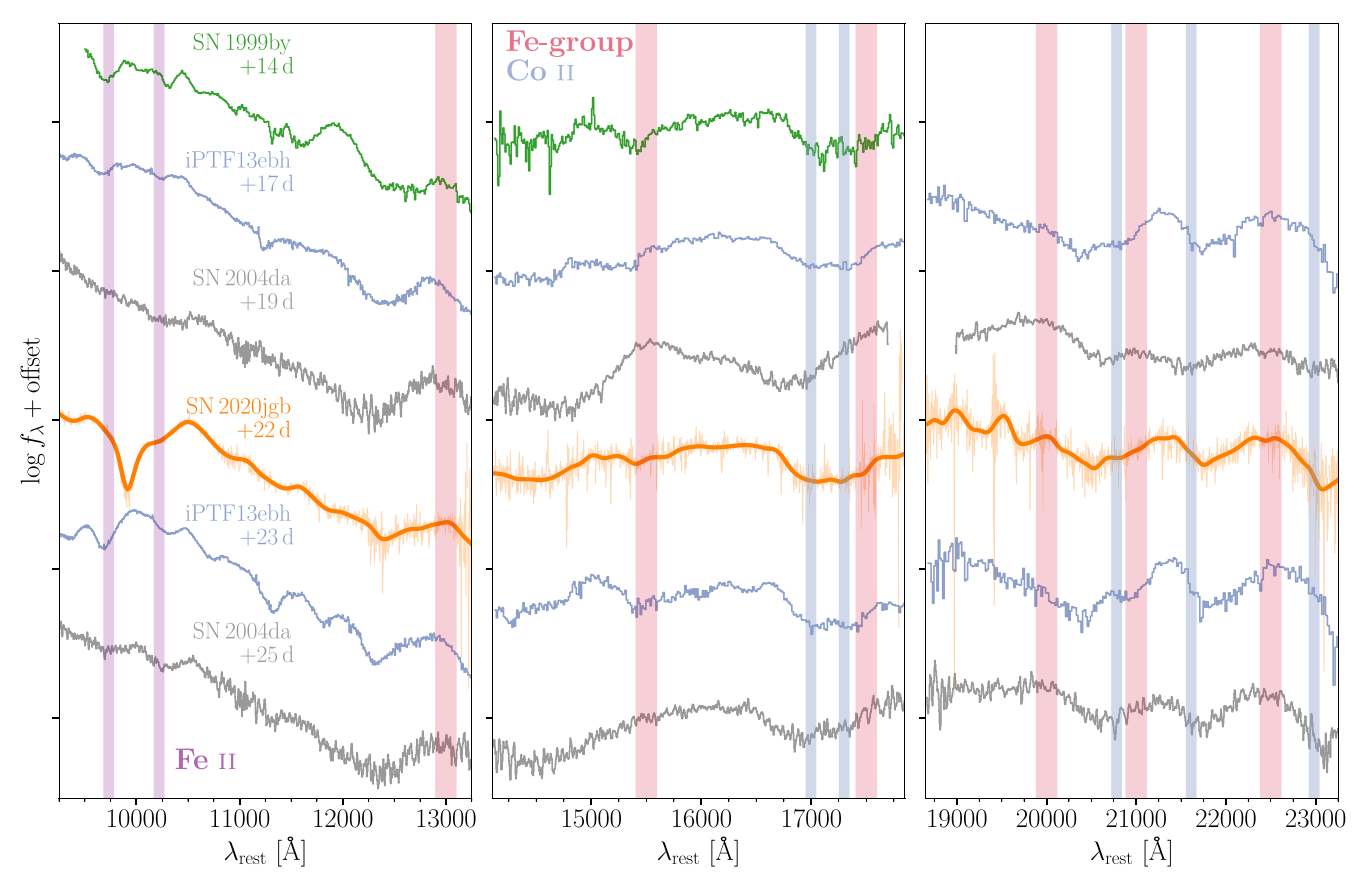


Figure 3. NIR spectra of SN 2020jgb, a normal-luminosity SNe Ia (SN 2004da; Marion et al. 2009), and two subluminous SNe Ia (SN 1999by and iPTF13ebh; Höflich et al. 2002; Hsiao et al. 2015), obtained 15–25 days after maximum brightness. All the objects show similar spectral features except for the absorption line near 1 μm. For each spectrum, the continuum at ≥1.2 μm is significantly reshaped by the line-blanketing from Fe-group elements (red stripes), which are continuous emission features composed of unresolved Fe-group lines peaking at ~1.30, 1.55, 1.75, 2.00, 2.10, and 2.25 μm (Marion et al. 2009). Between these peaks lie multiple strong Co II absorption lines (blue stripes), for which a typical post-maximum expansion velocity of 8000 km s⁻¹ is assumed. The purple stripes correspond to Fe II λ 9998 and Fe II λ 10500, also with an expansion velocity of 8000 km s⁻¹.

stay optically thick several weeks after maximum light. The Ca II IRT also exhibits similarly high velocities at the same phase (\sim 24,000 km s⁻¹), meaning that high-velocity absorption is not impossible at this phase. The expansion velocity in the ejecta is roughly linearly proportional to the radius, so such a high velocity indicates that both the Ca II IRT and the tentative He I absorption line form far outside the normal photosphere, which has a velocity of only \sim 10,000 km s⁻¹. The two-dimensional (2D) models of Kromer et al. (2010) also suggest that helium may expand faster than the synthesized calcium in the He-shell. In this sense, the He-shell DDet scenario is supported because any unburnt helium would be located in the outermost ejecta.

We cannot claim an unambiguous detection of He I, however, as our spectra lack definitive absorption from other He I features that we would expect to be prominent, such as He I $\lambda 20581$. Considering a line velocity of $\sim 26,000~\rm km~s^{-1}$ and a host-galaxy redshift of 0.0307, this line will be blueshifted to $\sim 1.95~\mu m$ in the observer frame, which overlaps with some strong telluric lines within $1.8-2.0~\mu m$. In this region our NIR spectrum has S/N ≈ 5 following telluric correction, yet we do not see any significant absorption feature. An upper limit of the equivalent width is determined to be <2% that of the He I $\lambda 10830$ line, while the $\lambda 20581$ line is theoretically supposed to be only a factor of 6–12 weaker, depending on the temperature (Marion et al. 2009). The observed 1 μ m feature in SN 2020jgb is as strong as the He I

 $\lambda10830$ line in many helium-rich Type Ib supernovae (SNe Ib, Shahbandeh et al. 2022). In SNe Ib, the He I $\lambda20581$ line is weaker than the He I $\lambda10830$ line, yet still prominent (Shahbandeh et al. 2022). In one of the models of Boyle et al. (2017), there is no obvious He I $\lambda20581$ absorption in the synthetic spectra (see their Figure 7), but the model is intended to be representative of normal-luminosity SNe Ia. If the 1 μm feature is associated with He I, it is unusual that we do not detect a corresponding feature around 2 μm .

Other possible identifications for the $1 \mu m$ feature include Mg II $\lambda 10927$, C I $\lambda 10693$, and Fe II $\lambda 10500$ and $\lambda 10863$. The Mg II $\lambda 10927$ line is prevalent in the NIR spectra of SNe Ia, but usually disappears within a week after peak brightness (Marion et al. 2009). In SN 2020jgb the 1 μ m feature was still visible more than a month after maximum light in the Keck/LRIS spectrum. An Mg II $\lambda 10927$ identification would require an absorption velocity of \sim 28,000 km s⁻¹, \sim 20% faster than the HVFs of the Ca II IRT at the same phase. Such a high-velocity Mg II line has never been seen in other SNe Ia, and requires a high magnesium abundance in the outermost ejecta. However, the amount of magnesium synthesized in the detonation of the He-shell is expected to be tiny (Fink et al. 2010; Kromer et al. 2010; Polin et al. 2019, 2021). On the other hand, if we attribute this 1 μ m feature to high-velocity Mg II, we would expect an even stronger Mg II λ 9227 line to be blueshifted to the red edge of the Ca II IRT, which is not detected. Given the

strength of the 1 μ m feature, the Mg II λ 9227 line should not be completely obscured by the Ca II IRT features.

C I $\lambda 10693$ is not observed as frequently as Mg II $\lambda 10927$ in SNe Ia. Hsiao et al. (2019) presented a sample of five SNe Ia with C I detections, showing that the C I feature is strongest for fainter, fast-declining objects. However, in their sample, the CI line is a pre-maximum feature that fades away as the luminosity peaks, so the discrepancy in phase is large. The required expansion velocity of \sim 22,000 km s⁻¹ is substantially faster than the estimated carbon velocity for the sample of Hsiao et al. (2019) $(\sim 10,000-12,000 \text{ km s}^{-1})$, but still consistent with the HVFs of the Ca II IRT in SN 2020jgb. Nonetheless, no significant carbon absorption is detected in the optical. It is also noteworthy that the amount of unburnt carbon is expected to be minimal in sub- M_{Ch} WDs ignited by He-shell detonation (Polin et al. 2019), in contrast to near- $M_{\rm Ch}$ WDs ignited by pure deflagration where the carbon burning could be incomplete. We therefore would not expect to detect any carbon features in an He-shell DDet SN.

The Fe II features in SNe Ia usually start to develop approximately three weeks after peak brightness, which is about the same phase as that at which we obtained our GNIRS spectrum. Two Fe II lines, $\lambda 9998$ and $\lambda 10500$, are actually visible on the blue/red wings of the $1 \mu m$ feature (see Figure 3). The Fe II $\lambda 10863$ line is not detected in the GNIRS spectrum. SN 2004da shows very similar Fe II features near 1 μ m, in which Fe II λ 10500 is the strongest line at this phase, as displayed in Figure 3. They correspond to an expansion velocity of $\sim 8000 \text{ km s}^{-1}$, which is consistent with the PVFs of the Ca II IRT at the same epoch. They also match the same two lines for normal SNe Ia (Marion et al. 2009), making the identification more reliable. Obviously, these two Fe II features are wider and shallower than the strong feature between them. We fit the 1 μ m feature with three Gaussian profiles. Two of them are set to be the blueshifted Fe II λ 9998 and λ 10500, and the other is an uncorrelated Gaussian profile that mainly describes the deep absorption feature in the center of the line complex. We find that the shallower and wider Fe II lines only make up $\sim 40\%$ of the total equivalent width, and the remaining \sim 60% comes from the central feature, which cannot be accounted for by any Fe II feature at the same velocity. Given the similarity of the Fe-group line-blanketing between the GNIRS spectrum and the spectrum of SN 2004da at +25 days, the distribution of Fe-group elements inside each SN ejecta should be somewhat similar, so the central region of the 1 μ m feature is not likely to be associated with Fe II either.

4. Discussion

4.1. Models

We model SN 2020jgb using the methods outlined by Polin et al. (2019); the process is twofold. After choosing an initial model that describes a WD of a given mass with a choice of He-shell mass, we use the CASTRO code (Almgren et al. 2010) to perform a 1D hydrodynamic simulation with simultaneous nucleosynthesis from the time of He-shell ignition through the secondary detonation and until the ejecta have reached homologous expansion (~10 s). At this point we take the ejecta profile (velocity, density, temperature, and composition) and use the Monte Carlo radiative transport code SEDONA (Kasen et al. 2006) to calculate synthetic light curves and spectra of our model under the assumption of LTE.

For He-shell DDet SNe, the peak luminosity in r_{ZTF} is a proxy for the amount of ⁵⁶Ni synthesized in the detonation, which reflects the total progenitor mass (C/O core + He-shell; Polin et al. 2019). We find that models with a total mass of $0.95\,M_\odot$ reproduce the r_{ZTF} -band peak brightness well if there is no extinction from the host galaxy. If the host galaxy reddens SN 2020jgb by $E(B-V)_{\rm host}=0.13$ mag, then specific luminosity in r_{ZTF} would be ~25% higher, and the corresponding progenitor mass would be roughly $1.00\,M_\odot$. The uncertainty in the extinction limits the precision with which the progenitor mass of SN 2020jgb can be constrained.

Nonetheless, the major photometric and spectroscopic features of SN 2020jgb are consistent with those of a DDet SN with a massive shell. In Figure 4, we show the comparison of the observations of SN 2020jgb with He-shell DDet models with a shell mass of $0.13 M_{\odot}$ and total masses of $0.95 M_{\odot}$ and $1.00 M_{\odot}$, respectively. To compare the models with the observations, we apply the adopted host reddening $(E(B-V)_{host} = 0.0$ or 0.13 mag) to the rest-frame model SN spectrum, then redshift the model spectrum by 0.0307, before applying Galactic reddening $(E(B-V)_{MW} = 0.404 \text{ mag})$. Both models reproduce the overall evolution of SN 2020jgb in r_{ZTF} , but fail to provide a reasonable fit to the light curve in g_{ZTF} . Specifically, the peak brightness in $g_{\rm ZTF}$ is overestimated in the $0.87\,M_{\odot} + 0.13\,M_{\odot}$ model but underestimated in the $0.82 M_{\odot} + 0.13 M_{\odot}$ model. The overall g_{ZTF} -band light curves in both models evolve faster than our observations, and quickly become ≥1 mag fainter than the observed g_{ZTF} brightness at the same epoch.

The spectral comparison reveals more details. We find that both models, especially the $0.82 M_{\odot} + 0.13 M_{\odot}$ one, provide a reasonable match to the ALFOSC spectrum obtained ~4 days prior to the peak at rest-frame wavelengths ≥5500 Å. The same is true for the SEDM spectrum obtained ~4 days after maximum brightness, though both models overpredict flux excess in the Ca II IRT P-Cygni profile. Meanwhile, both models provide a poor fit to the observation in bluer regions. Before maximum brightness in the observation, the $0.87 M_{\odot} + 0.13 M_{\odot}$ model exhibits weaker Fe-group lineblanketing, thus showing a much higher total flux in g_{ZTF} . The $0.82\,M_{\odot} + 0.13\,M_{\odot}$ model provides a proper level of lineblanketing, but the continuous absorption in the synthetic spectrum terminates at a longer wavelength (\sim 5400 Å, as opposed to \sim 5200 Å in the spectrum at -4 days). As we have already mentioned in Section 3.1 when discussing K-corrections, the observed flux in g_{ZTF} is extremely sensitive to the red edge of the line-blanketing region, which, in the observer frame, is close to the edge of the filter. Figure 4 shows that while f_{λ} peaks in the g_{ZTF} filter near maximum light, in the $0.82\,M_{\odot} + 0.13\,M_{\odot}$ model the synthetic f_{λ} peaks in the gap between the g_{ZTF} and r_{ZTF} filters. The same is true for the $0.87\,M_{\odot} + 0.13\,M_{\odot}$ model after the $r_{\rm ZTF}$ -band peak. Interestingly, this mismatch is also seen when fitting similar DDet models to SN 2018byg (see Figure 6 in De et al. 2019) despite the convincing match to observations at longer wavelengths, suggesting this is one of the systematics in our models. By manually shifting the synthetic spectra at -4 days in the $0.82 M_{\odot} + 0.13 M_{\odot}$ model blueward by 200 Å, we find that the corresponding synthetic magnitude in gZTF immediately increases by ~ 0.5 mag. Given the sensitivity of brightness in g_{ZTF} on modeling the line-blanketing and the uncertainty in our models from Polin et al. (2019), we do not attempt to fit the g_{ZTF}-band light curve of SN 2020jgb even near maximum light.

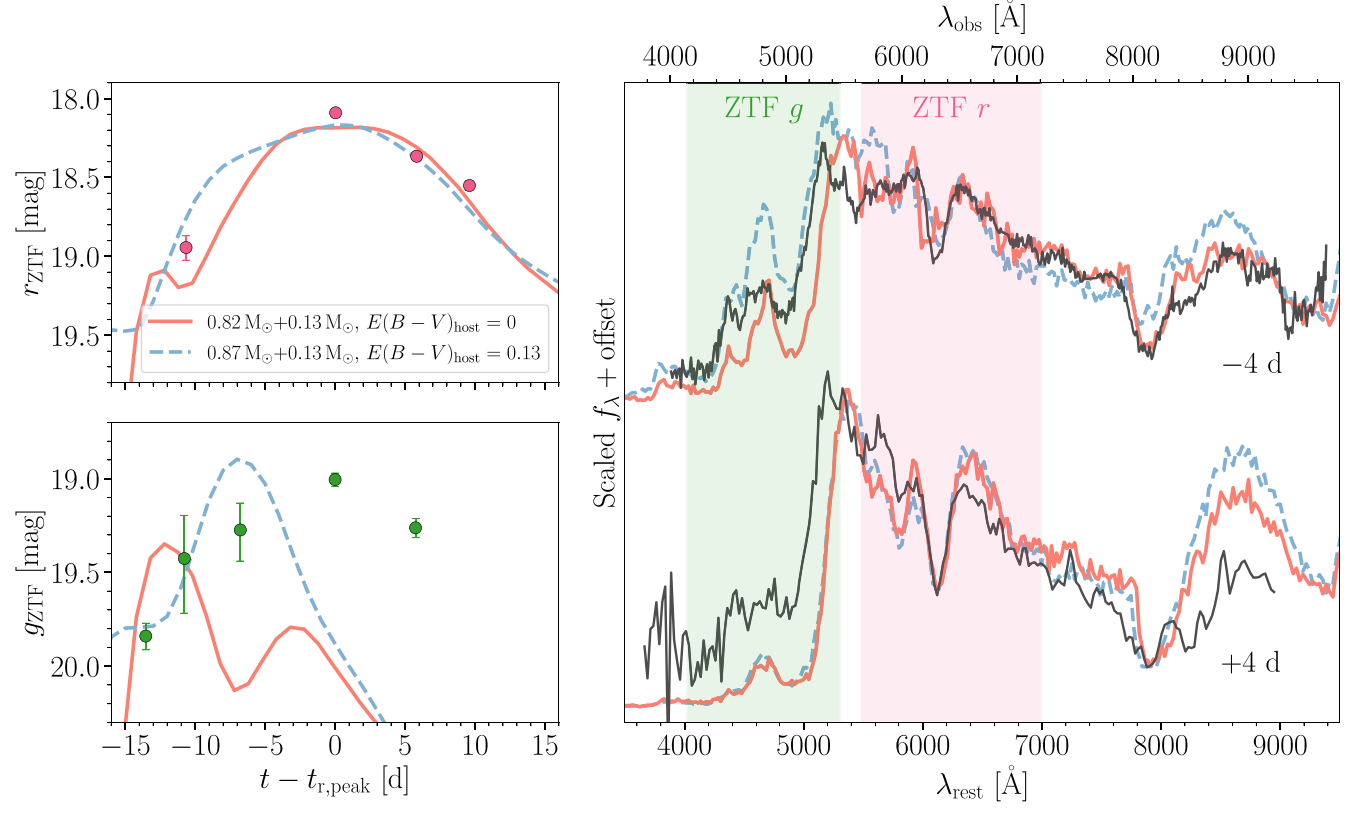


Figure 4. Spectrophotometric comparison of observations of SN 2020jgb with two He-shell DDet models using the methods described in Polin et al. (2019). For the $0.82~M_{\odot}+0.13~M_{\odot}$ model, only the Galactic reddening of $E(B-V)_{\rm MW}=0.404$ mag is applied to the synthetic spectra and photometry; for the $0.87~M_{\odot}+0.13~M_{\odot}$ model, additional reddening of $E(B-V)_{\rm host}=0.13$ mag from the host galaxy is assumed. Left: comparison of the ZTF photometry with the synthetic light curves. The model parameters are indicated in the legend as (C/O core mass + He-shell mass). The upper (lower) panel shows the evolution in $r_{\rm ZTF}$ ($g_{\rm ZTF}$). The phases have been rescaled to the rest frame of the host galaxy. Right: comparison of the observed spectra with the models around maximum brightness. The shaded regions correspond to the coverage of the ZTF g and r filters with transmission above half-maximum. All spectra are normalized such that they would have the same synthetic brightness in $r_{\rm ZTF}$. The synthetic spectra are further binned with a size of 20 Å.

The systematics in modeling the line-blanketing (and the flux in many similar g bands) may be attributed to a variety of factors on handling the explosion and radiative transfer. First, our models assume LTE, which is not valid once the ejecta become optically thin. Typically the bulk ejecta of a sub- $M_{\rm Ch}$ SN Ia remain optically thick for \sim 30 days after the explosion. But in modeling the g_{ZTF} -band brightness, the LTE assumption is more challenging because the major opacity in g_{ZTF} comes from the Fe-group line-blanketing in the outermost ejecta, where the optical depth may evolve differently from that near the photosphere. Hence, the LTE condition may become inapplicable much earlier. Furthermore, our 1D He-shell model is not capable of capturing multidimensional effects in the explosion such as asymmetries. The viewing angle is known to have a significant influence on the observed light curves (Kromer et al. 2010; Sim et al. 2012; Gronow et al. 2020; Shen et al. 2021), especially in bluer bands where the line-blanketing depends sensitively on the distribution of He-shell ashes (Shen et al. 2021). In previous studies of other He-shell DDet objects, the g-band brightness is systematically underpredicted shortly after the peak, despite the fact that redder bands can be fit decently (e.g., Jiang et al. 2017; Jacobson-Galán et al. 2020).

Another discrepancy occurs in the late-time spectra. It is argued in Polin et al. (2021) that as the total progenitor mass in the He-shell DDet decreases, the SN gets fainter and the major coolants in the nebular phase change smoothly from Fe-group elements to the [Ca II] $\lambda\lambda$ 7291, 7324 doublet. For a total

progenitor mass $\lesssim 1.0 \, M_{\odot}$, [Ca II] emission features are expected to dominate Fe-group features in the nebular phase, clearly in contrast to what we see in SN 2020jgb. Since there is no evidence that the progenitor mass of SN 2020jgb is strongly underestimated (e.g., due to substantial host extinction that has not been accounted for), the absence of [Ca II] emission features suggests the transition between the Fe-strong and Castrong regimes may occur for a lower progenitor mass than simulations have predicted. As for other peculiar DDet events, SN 2016hnk is estimated to have an even lower progenitor mass ($\sim 0.87 \, M_{\odot}$; Jacobson-Galán et al. 2020) and shows [Ca II] lines indisputably, drawing a lower limit of the progenitor mass for this transition (see Galbany et al. 2019, for discussion on the potential host-galaxy extinction on SN 2016hnk). The late-time spectrum of SN 2019ofm also exhibits prominent [Ca II] emission.³⁴ SN 2018byg and SN 2016dsg were not observed in the nebular phase, so it remains unknown whether they exhibit [Ca II] emission, which would otherwise be expected to show up at $\sim +150$ days.

Given the strong match in the $r_{\rm ZTF}$ -band light curves and the near-peak spectra at wavelengths $\gtrsim 5500\,\rm \AA$ between the observations of SN 2020jgb and our He-shell DDet models

³⁴ For this reason, SN 2016hnk and SN 2019ofm also fall into the category of the calcium-rich (Ca-rich) transients, which are well known for their conspicuous nebular [Ca II] emission (Filippenko et al. 2003; Perets et al. 2010; Kasliwal et al. 2012). The strong [Ca II] emission in the nebular phase may be explained by an He-shell DDet explosion (Dessart & Hillier 2015; Polin et al. 2019). See De et al. (2020) for a detailed discussion.

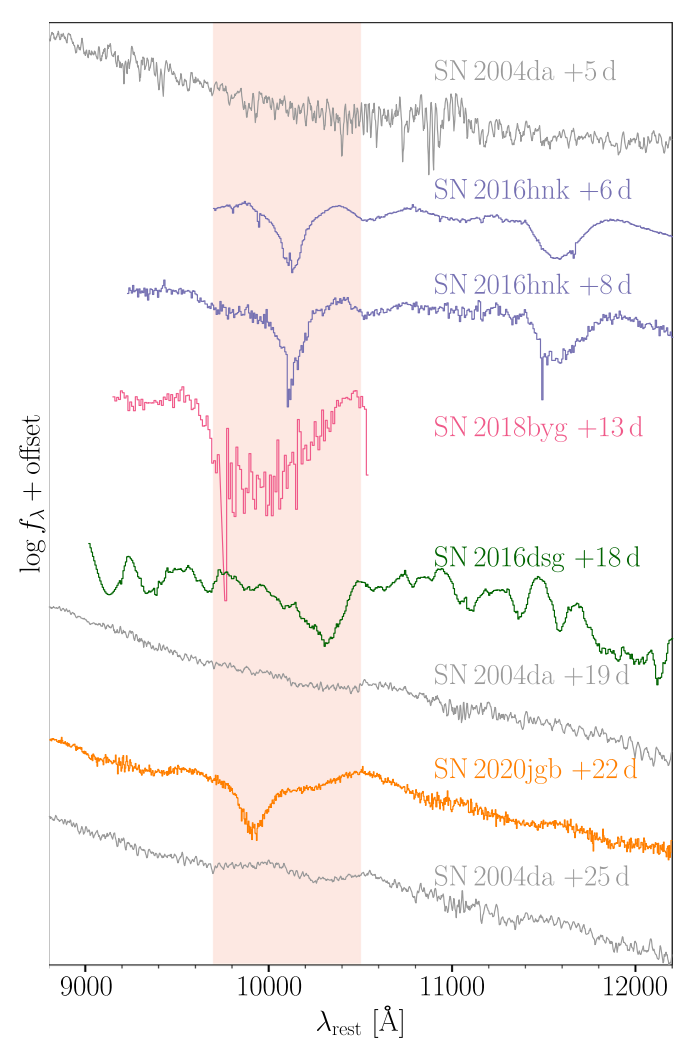


Figure 5. NIR spectra of normal SNe Ia SN 2011fe (Mazzali et al. 2014) and SN 2004da (Marion et al. 2009) and four subluminous SNe Ia as He-shell DDet candidates—SN 2016dsg (Dong et al. 2022a), SN 2016hnk (Galbany et al. 2019), SN 2018byg (De et al. 2019), and SN 2020jgb (this work). All He-shell DDet candidates show prominent absorption near 1 μ m (the highlighted region). The spectrum of SN 2018byg is originally noisy, so it is binned with a size of 10 Å. For SN 2016dsg, we show the spectrum smoothed with a Savitzky–Golay filter in Dong et al. (2022a).

following Polin et al. (2019), we conclude that SN 2020jgb is consistent with a DDet event ignited by a massive He-shell. Our 1D LTE models cannot characterize the Fe-group line-blanketing effects accurately, leading to large uncertainty in the shell mass. Readers are referred to the Appendix, where we show the comparison of our observations to models with a variety of shell masses, in which the thinner-shell models (shell masses $<0.1\,M_\odot$) cannot reproduce the properties of SN 2020jgb. Depending on the extinction in the host galaxy, the total mass of the progenitor should be $\sim 0.95-1.00\,M_\odot$. To constrain the progenitor masses of additional He-shell DDet SNe to a higher precision, one should thoroughly discuss any potential host extinction. Multidimensional simulations with more realistic radiative transfer setups are necessary to resolve the systematics in our current models.

4.2. The 1 µm Feature

While the nature of the 1 μ m feature remains uncertain, other He-shell DDet candidates show similar complexity in this

region. In the currently small sample, only four objects (SN 2016dsg, SN 2016hnk, SN 2018byg, and SN 2020jgb) have at least one available NIR spectrum (all obtained at different phases), vet each exhibits a strong absorption feature near 1 μ m. as shown in Figure 5. SN 2016hnk has two deep absorption features at \sim 1.01 μ m and \sim 1.16 μ m. It is suggested in Galbany et al. (2019) that both of them are caused by Fe II, though they are deeper than in other SNe Ia. If the 1 μ m feature is associated with He I, the expansion velocity would be \sim 21,000 km s⁻¹. For SN 2016dsg, the minimum of the $1 \mu m$ feature is around $\sim 1.03 \,\mu \text{m}$, with a corresponding velocity of $\sim 15,000 \,\text{km s}^{-1}$. The large width and low S/N for the $1 \mu m$ feature in SN 2018byg make it difficult to determine an exact line velocity, suggesting that feature may be a mixture of several different lines. Interestingly, all these 1 μ m features, assuming an He I origin, show an expansion velocity consistent with the HVF of the Ca II IRT (see Figure 6). The variation in Ca II velocities is large (\sim 15,000–25,000 km s⁻¹), probably due to different viewing angles (Fink et al. 2010; Shen et al. 2021). The PVFs of the Ca II IRT of these He-shell DDet candidates show a similar expansion velocity of \sim 10,000 km s⁻¹.

Unfortunately, none of the spectra of SN 2016dsg, SN 2016hnk, or SN 2018byg cover the 2 μ m region; thus, it is not possible to identify the presence of helium decisively. But if the 1 μ m features of these objects are of the same origin, they are more likely to be correlated with the high-velocity ejecta lying in the outmost region in the SNe, because at least for SN 2020jgb, SN 2016dsg, and SN 2016hnk, the difference in their photospheric velocities cannot explain the discrepancy in their line velocities of the 1 μ m feature. Then helium is still a promising candidate to cause strong absorption near 1 μ m for these subluminous He-shell DDet SNe Ia.

In conclusion, every peculiar He-shell DDet candidate with available NIR spectra displays a strong absorption feature near 1 μ m. This feature is not seen in normal SNe Ia. Interestingly, the available NIR spectra are all obtained at different epochs, suggesting that this feature may be long-lived. If the feature is due to He I, then DDet explosions exhibit a wide diversity in the expansion velocity. While it remains to be confirmed in a larger sample, we speculate that anomalously strong absorption around 1 μ m is a distinctive attribute of peculiar He-shell DDet SNe.

4.3. The Host Environment of He-shell DDet SNe

We model the host galaxy of SN 2020jgb (see Figure 7) using prospector (Johnson et al. 2021), a package for principled inference of stellar population properties using photometric and/or spectroscopic data. Prospector applies a nested sampling fitting routine through dynesty (Speagle 2020) to the observed data and produces posterior distributions of the stellar population properties and model SEDs with use of Python-FSPS (Conroy et al. 2009; Conroy & Gunn 2010). Our observed data include the Galactic-extinction-corrected DEIMOS spectrum, as well as the archival photometric data from the Panoramic Survey Telescope and Rapid Response System (Pan-STARRS; Chambers et al. 2016, g, r, i, z, y Kron magnitudes) and the VISTA

 $[\]overline{^{35}}$ We also note that a similar 1 μ m feature is detected in another possibly relevant object, SN 2012hn (Valenti et al. 2014), in an NIR spectrum obtained at +25 days. SN 2012hn is a Ca-rich transient exhibiting weak Si II lines and no optical helium features. It shows similar spectral properties (e.g., Fe-group line-blanketing) to those of SN 2016hnk and SN 2019ofm (De et al. 2020). This indicates a possible He-shell DDet origin of SN 2012hn.

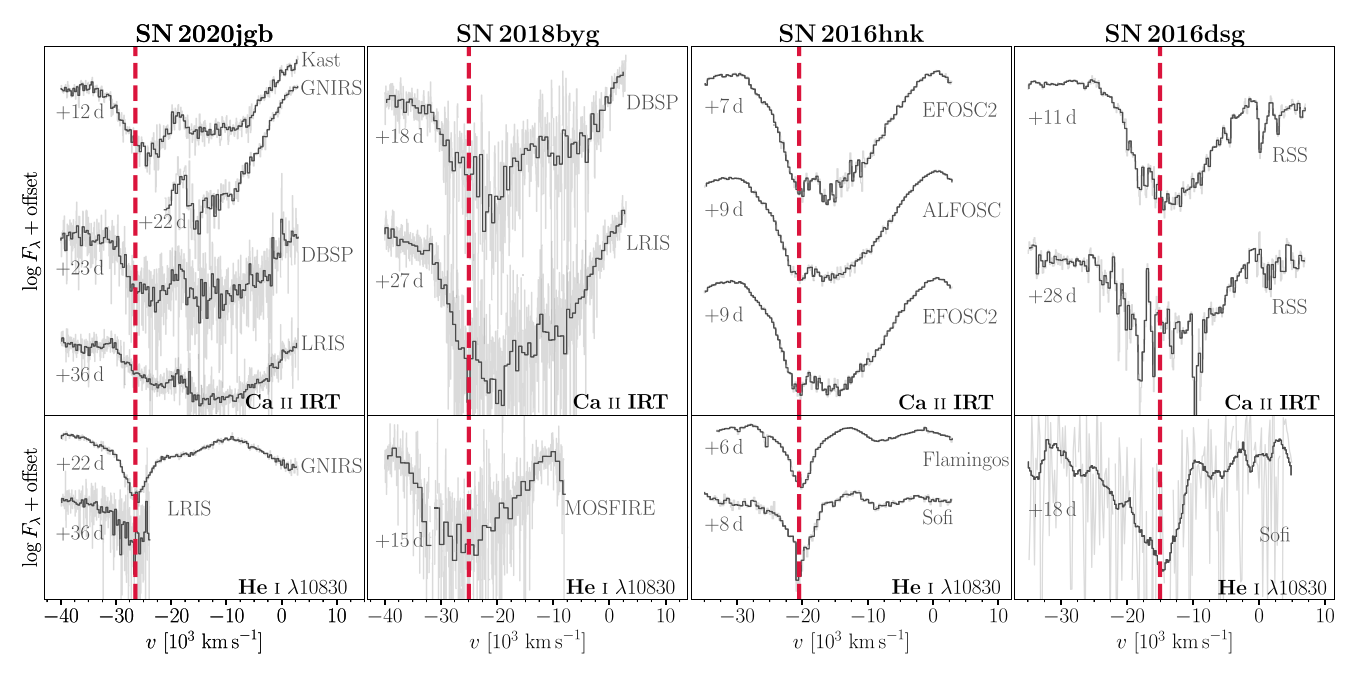


Figure 6. Spectra of SN 2020jgb, SN 2018byg (De et al. 2019), SN 2016hnk (Galbany et al. 2019), and SN 2016dsg (Dong et al. 2022a) in velocity space, showing the similarity in expansion velocities of the 1 μ m features (lower panels) with the Ca II IRT absorption features (upper panels), assuming the 1 μ m features are associated with He I λ 10830. The red dashed lines mark the minimum of each 1 μ m feature, which are displayed to guide the eye.

Hemisphere Survey (VHS; McMahon et al. 2013, J and K_s Petrosian magnitudes). We use a parametric delayed- τ star formation history, given by Equation (1) of Nugent et al. (2020) and defined by the e-folding factor τ , the Galactic dust extinction law (Cardelli et al. 1989), and the Chabrier initial mass function (Chabrier 2003) to the model. We further apply a massmetallicity relation (Gallazzi et al. 2005) to sample realistic stellar masses and metallicities and a dust law that ensures young stellar light attenuates dust twice as much as old stellar light, as has been observed. We also add a nebular emission model (Byler et al. 2017) with a gas-phase metallicity and a gas ionization parameter to correctly measure the strength of the emission lines in the DEIMOS spectrum. The model spectral continuum is built from a tenth-order Chebyshev polynomial. We determine the stellar mass and star formation rate (SFR) from the prospector output, as shown by Nugent et al. (2022). The estimated stellar mass is $\log(M_* [M_{\odot}]) = 7.79^{+0.07}_{-0.06}$, and the specific star formation rate (sSFR) is $\log(\text{sSFR [yr}^{-1}]) = -10.25^{+0.09}_{-0.08}$, with the uncertainties denoting the 68% highest posterior density regions.

In Figure 8, we show the sSFR and the stellar mass for the host galaxies of six He-shell DDet candidates. Again using prospector, we fit the stellar properties for all the other candidates with optical spectra from the Sloan Digital Sky Survey (SDSS; York et al. 2000) and photometry from Data Release 9 (DR9) of the DESI Legacy Imaging Surveys (LS; Dey et al. 2019, g, r, z, W_1 , W_2 , W_3 , W_4 magnitudes). With mid-infrared (MIR) photometry available, prospector can better estimate the overall dust extinction in the host galaxy and the contribution of an active galactic nucleus (AGN) to the SED. We therefore add two additional parameters to our

prospector fit to sample the MIR optical depth and fraction of the total galaxy luminosity due to an AGN.

Unfortunately, two hosts (those of SN 2016hnk and SN 2019ofm) are nearby $(z \le 0.03)$ late-type galaxies with extended, spatially resolved spiral structures. Examination of the photometry model from Legacy Surveys (LS) shows that the galaxy aperture does not include the blue, diffuse star-forming regions of these galaxies. Fitting the SDSS spectra + LS photometry would inevitably underestimate their sSFR. For the host of SN 2016hnk, we instead adopt the results of Dong et al. (2022b), which are based on broadband far-ultraviolet to farinfrared photometry from the z = 0 Multiwavelength Galaxy Synthesis I (z0MGS; Leroy et al. 2019) to characterize the stellar population with prospector. The SFR they estimated is 1.1 dex higher than ours, suggesting intense star formation in the spiral arms. For the host of SN 2019ofm, there are no archival stellar population data available; so we redo the photometry using science-ready coadded images from the Galaxy Evolution Explorer (GALEX) general release 6/7 (Martin et al. 2005, FUV and NUV bands), SDSS DR9 (Ahn et al. 2012, u, g, r, i, z bands), the Two Micron All Sky Survey (2MASS; Skrutskie et al. 2003, 2006, H and J bands), and preprocessed Wide-field Infrared Survey Explorer (WISE) images (Wright et al. 2010) from the unWISE archive (Lang 2014, W_1 and W_2 bands).³⁷ We use the software package LAMBDAR (Lambda Adaptive Multi-Band Deblending Algorithm in R) (Wright 2016) and tools presented in Schulze et al. (2021) to measure the total brightness of the host galaxy. But with the LAMBDAR photometry, the estimated SFR is essentially the same as in the previous fit, suggesting that there is not much ongoing star formation in the spiral arms. This, along with its moderate

 $^{^{36}}$ LS DR9 includes MIR (W_1 – W_4) fluxes from images through year 6 of NEOWISE-Reactivation (https://wise2.ipac.caltech.edu/docs/release/neowise/neowise_2020_release_intro.html) force-photometered in the unWISE (Meisner et al. 2017a, 2017b; UnWISE Team 2021) maps at the locations of LS optical sources.

³⁷ The unWISE images are based on the public WISE data and include images from the ongoing NEOWISE-Reactivation mission R3 (Mainzer et al. 2014; Meisner et al. 2017a), available on http://unwise.me.

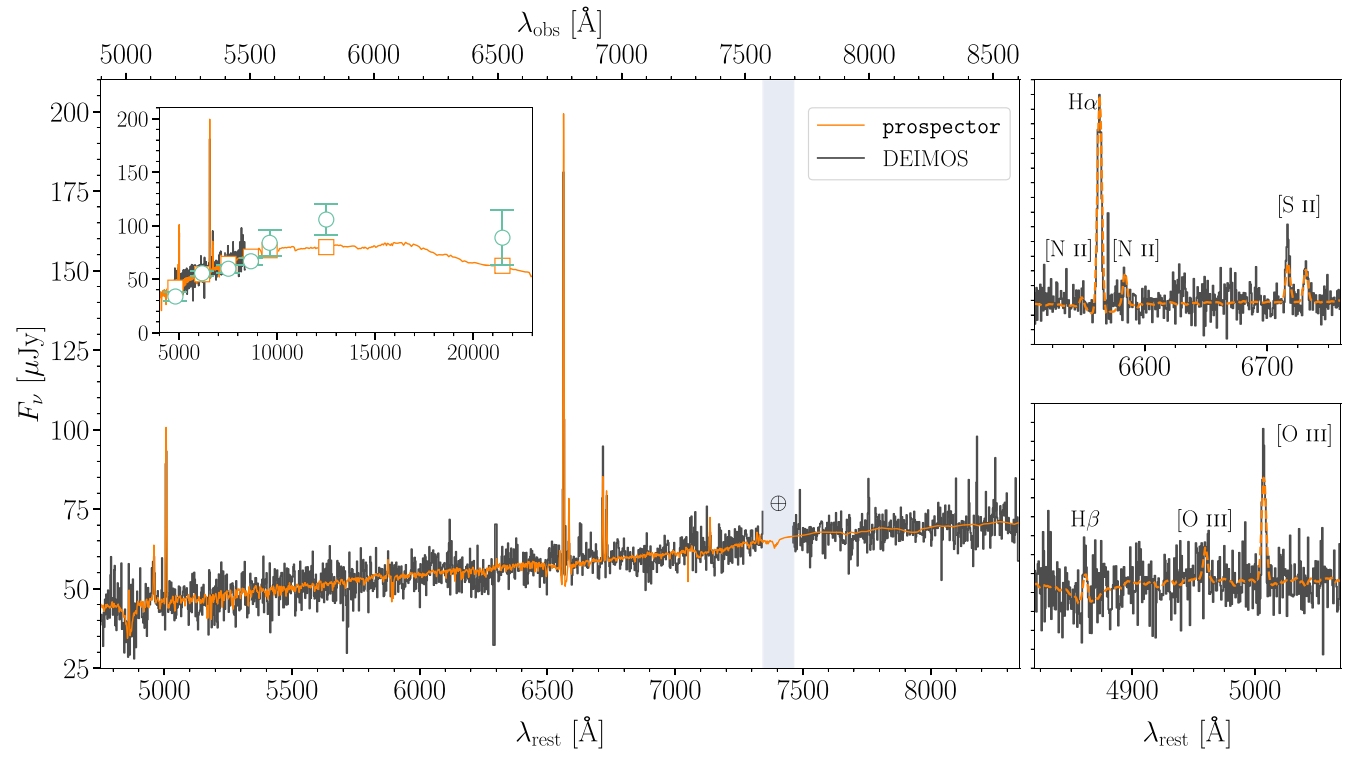


Figure 7. The SED of the star-forming dwarf galaxy PSO J175312.663+005122.078 (the host galaxy of SN 2020jgb) and the model from prospector. When fitting the SED with prospector, the DEIMOS spectrum is automatically rescaled to fit the archival photometry from Pan-STARRS (Chambers et al. 2016, g, r, i, z, y Kron magnitudes) and VHS (McMahon et al. 2013, J and K_s Petrosian magnitudes). Left: the SED in the optical band (4750–8350 Å in the rest frame of the host galaxy). The black line corresponds to the observed spectrum, binned with a size of 2 Å. The orange line is the prospector model produced from the median of the posterior distributions of the stellar population properties. The blue shaded region is masked in the fitting owing to the strong telluric lines. The inset shows the same comparison, but covering the g through K_s bands (4000–24,000 Å). Apart from the spectra, we also show the multiband photometry (green circles) and the best-fit magnitudes (orange squares). Right: spectra around the most prominent emission lines. Top right: Hα, [N II] $\lambda\lambda$ 6548, 6583, [S II] $\lambda\lambda$ 6716, 6731. Bottom right: Hβ, [O III] $\lambda\lambda$ 4959, 5007.

sSFR $(\log(sSFR [yr^{-1}]) = -11.27)$, indicates the host galaxy is in the transitional phase.

In addition, the host of the normal SN Ia SN 2018aoz (NGC 3923) is a local (z=0.00580) early-type galaxy and is outside the SDSS footprint, so we adopt its stellar population properties from the Census of the Local Universe (CLU) catalog (Cook et al. 2019; De et al. 2020). Nonetheless, it is close to several extended sources with low surface brightness, which could be faint dwarf galaxies (see Figure 3 in Kasliwal et al. 2012). Its nebular-phase spectrum exhibits $H\alpha$ emission, which indicates potential star formation, but could also be explained with photoionized gas around the transient (Kasliwal et al. 2012).

Figure 8 reveals that He-shell DDet SNe emerge in both star-forming and passive galaxies. There is also significant diversity in their location within their host galaxy. SN 2020jgb has a small projected physical offset (~0.2 kpc) from the center of its host, a star-forming dwarf galaxy, so it is likely to originate from a young, star-forming environment. SN 2016hnk has a moderate projected host offset (~4 kpc) and a potential origin in an H II region with ongoing star formation (Galbany et al. 2019). SN 2019ofm has a large projected offset (~11 kpc) but is still on a spiral arm, as shown in its DECaLS image (Dey et al. 2019). Other objects, including the recently reported SN 2016dsg and OGLE-2013-SN-079 (Dong et al. 2022a), show large projected host offsets (\gtrsim 10 kpc) and lie in the galaxy outskirts, which usually indicates an old stellar population origin.

In this sense, the He-shell DDet sample resembles the normal SN Ia population, which can occur in both star-forming and quenched galaxies (e.g., Sullivan et al. 2006; Smith et al. 2012). This is very different from some other types of thermonuclear SNe such as 02cx-like SNe, which almost only appear in star-forming galaxies, or 91bg-like and 02es-like objects, which prefer old stellar environments (see the review by Jha et al. 2019). This favors the postulated sequence that He-shell DDet SNe may make up a substantial fraction of normal SNe Ia, and is supported by observations of stellar metallicity (Sanders et al. 2021; Eitner et al. 2022).

The diversities in host environments indicate multiple formation channels in the He-shell DDet SN population. Those in star-forming galaxies, SN 2020jgb being the most unambiguous example, could originate from some analogues of the two subdwarf B binaries with WD companions (Iben et al. 1987; Geier et al. 2013; Kupfer et al. 2022) discovered in young stellar populations. On the other hand, those with large host offsets could not be easily formed in situ. Similarly, many Ca-rich transients (Filippenko et al. 2003; Perets et al. 2010; Kasliwal et al. 2012) are also observed in remote locations (e.g., Lunnan et al. 2017), for which some dynamical formation channels have been proposed (Lyman et al. 2014). To reach the outskirts of galaxies, WD binaries would need to be ejected by globular clusters (Shen et al. 2019) or supermassive black holes (Foley 2015) before explosion. Given that some Ca-rich transients show characteristic DDet properties (De et al. 2020),

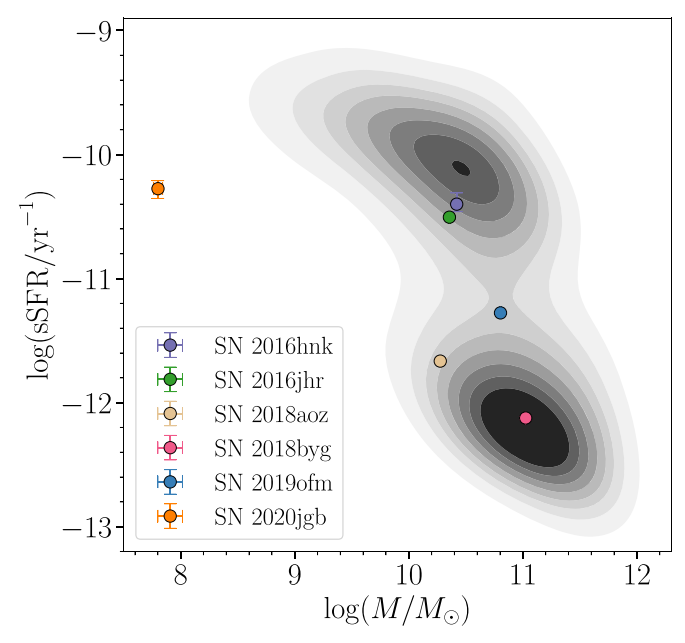


Figure 8. The sSFR and stellar mass for the host galaxies of He-shell DDet candidates, showing that He-shell DDet SNe can emerge in both star-forming and passive galaxies. The properties of the hosts of SN 2016hnk and SN 2018aoz are taken from Dong et al. (2022b) and the CLU catalog (Cook et al. 2019; De et al. 2020), respectively. The gray contours correspond to the bivariate distributions of stellar mass and sSFR for galaxies in the SDSS MPAJHU DR8 catalog (Kauffmann et al. 2003; Brinchmann et al. 2004), visualized using kernel density estimation with the data visualization library seaborn (Waskom 2021). Galaxies with BPT classification as AGNs or LINERs are excluded, since certain spectral features (e.g., $H\alpha$ emission) due to nuclear activity might be misinterpreted as being caused by star formation.

these channels may also be applicable to some of the He-shell DDet SNe.

The robust detection of SN 2020jgb in a star-forming region also agrees with independent studies of SN Ia progenitors using observations of stellar metallicity. After measuring the manganese abundance in the Sculptor dwarf spheroidal galaxy, it is argued in de los Reyes et al. (2020) that sub- $M_{\rm Ch}$ SNe Ia dominate the initial chemical enrichment of a galaxy, while near- $M_{\rm Ch}$ SNe become more important at later times. This indicates that, observationally, sub- $M_{\rm Ch}$ SNe Ia might have a stronger preference toward younger stellar populations than near- $M_{\rm Ch}$ SNe Ia. We note that while SN 2020jgb is the first confirmed subluminous He-shell DDet SN in a star-forming dwarf, which indicates that peculiar He-shell DDet SNe might be intrinsically rare, the same may not be true for the potential population of normal SNe Ia ignited by a DDet (Magee et al. 2021). A red flux excess, the hallmark of an He-shell detonation in a normal SN Ia, will only be evident in the first few days after the explosion, while few SNe Ia have been observed at such an early phase to date; thus, we might have missed a great number of normal He-shell DDet SNe. A systematic study based on prompt follow-up observations of infant SNe Ia will help verify this implication.

5. Conclusions

We have presented observations of SN 2020jgb, a peculiar SN Ia. It has a low luminosity, red $g_{ZTF}-r_{ZTF}$ colors, and strong line-blanketing in the optical spectra near maximum light. These observational properties are very similar to those of SN 2018byg (De et al. 2019), which could be explained by the

detonation of a shell of helium on a sub- $M_{\rm Ch}$ WD. Fitting the light curves of SN 2020jgb to a grid of models from Polin et al. (2019), we show that a \sim 0.82 M_{\odot} WD beneath a \sim 0.13 M_{\odot} He-shell provides a reasonable match to the peak-time spectrophotometric properties of SN 2020jgb. The systematics in our radiative transfer models, however, result in significant uncertainty in the shell mass. The uncertainty in the host galaxy extinction also limits the precision on estimating total progenitor mass, with a reasonable upper limit being \sim 1.00 M_{\odot} .

A high-S/N NIR spectrum obtained three weeks after maximum light exhibits a prominent absorption feature near $1 \mu m$, which could be produced by the unburnt helium (He I $\lambda 10830$) in the outermost ejecta expanding at a high velocity $(\sim 26,000 \,\mathrm{km \, s^{-1}})$. At the same epoch, the Ca II IRT also has similarly high velocities ($\sim 24,000 \,\mathrm{km \, s^{-1}}$). To date, NIR spectra have been observed for only a handful of candidate He-shell DDet SNe. Interestingly, all of them show deep absorption features near $1 \mu m$, which, if assumed to be He I $\lambda 10830$, would be expanding at a very similar velocity to the HVFs of the Ca II IRT. For these candidates the Ca II HVFs and putative He I velocities show significant diversity, ranging from $\sim 15,000 \, \text{km s}^{-1}$ in SN 2016dsg to $\sim 24,000 \, \text{km s}^{-1}$ in SN 2020jgb. If it is the unburnt helium and the newly synthesized calcium from the He-shell that produce these line features, such a consistency in the expansion rates of different absorption lines would be naturally explained. However, we could not find unambiguous evidence for other He I absorption lines, such as He I λ 20581, so we cannot claim a definitive detection of helium in SN 2020jgb. Nonetheless, alternative possibilities (Mg II, C I, Fe II) that may cause the 1 μ m feature are deemed even less likely. Helium is thus the most plausible explanation for the apparently ubiquitous 1 μ m features.

We propose that He-shell DDet SNe can be robustly identified with NIR spectra. For transients showing a clear 1 μ m feature, its potential association with He I $\lambda 10830$ could be tested by following the checklist below.

- 1. Search for He I $\lambda 20581$. A caveat is that one should not always expect to see significant He I $\lambda 20581$ absorption in He-shell DDet SNe, since this line is weaker than He I $\lambda 10830$ and could be almost invisible when the He-shell is thin (Boyle et al. 2017). Strong telluric lines near 2 μ m can make it difficult to detect He I $\lambda 20581$.
- 2. Calculate the line velocity assuming the feature is He I $\lambda 10830$ and check whether the speed is comparable with the Ca II IRT HVFs at a similar phase. While both the detonation recipe and viewing angles would affect the observed He I/Ca II velocity, we still expect both elements to expand at similar speeds along the line of sight if they both have an He-shell origin.
- 3. Exclude the possibility of other strong lines. If the NIR spectrum is obtained before the peak brightness of the SN, strong Mg II and C I absorption (Hsiao et al. 2019) would be possible contaminants. Otherwise, if the 1 μ m feature is seen in the transitional-phase spectrum when the inner region of the SN becomes visible, we need to carefully rule out the possibility of an Fe II origin (Marion et al. 2009).

The small, but growing, sample of He-shell DDet SNe are heterogeneous in their observational properties, including peak luminosity, color evolution, chemical abundances, and line velocities, which could be explained by a large variety of Heshell and WD masses (Polin et al. 2019; Shen et al. 2021), viewing angles (Shen et al. 2021), and the initial chemical compositions in the He-shell (Kromer et al. 2010). In addition, they are discovered in both old and young stellar populations, SN 2020jgb being the first unambiguous peculiar He-shell DDet candidate in a star-forming dwarf galaxy. If, as has been argued (e.g., Sanders et al. 2021; Eitner et al. 2022), a substantial fraction of normal SNe Ia are triggered by He-shell DDets, then we would naturally expect He-shell DDet SNe to emerge in both star-forming and passive galaxies. Our discovery of SN 2020jgb in a star-forming dwarf galaxy confirms that He-shell DDet events occur in a variety of different galaxies. This is unlike some other subtypes of SNe Ia (Jha et al. 2019), which strongly prefer either star-forming galaxies (e.g., SNe Iax) or passive galaxies (e.g., 91bg-like and 02es-like objects). Nonetheless, it remains to be examined whether peculiar He-shell DDet SNe stem from similar progenitors to the normal SNe Ia triggered by a DDet, or whether their massive He-shells could only be developed in a completely distinctive population of binary systems.

We thank the anonymous referee for a thoughtful and detailed report. We thank Eddie Schlafly and Dustin Lang for suggesting photometry from DESI Legacy Imaging Surveys in SED fitting. We are grateful to Aishwarya Dahiwale, Jillian Rastinejad, and Yuhan Yao for the high-quality spectra they obtained. We also appreciate the excellent assistance of the staffs of the various observatories where data were obtained. K. D. acknowledges support from NASA through the NASA Hubble Fellowship grant #HST-HF2-51477.001 awarded by the Space Telescope Science Institute, which is operated by the Association of Universities for Research in Astronomy, Inc., for NASA, under contract NAS5-26555. A.V.F. is grateful for financial support from the Christopher R. Redlich Fund and many other individual donors. K.M. is funded by the EU H2020 ERC grant No. 758638. S.S. acknowledges support from the G.R.E.A.T research environment, funded by Vetenskapsrådet, the Swedish Research Council, project No. 2016-06012. This work was also supported by the GROWTH project (Kasliwal et al. 2019) funded by the National Science Foundation (NSF) under grant 1545949.

This work is based on observations obtained with the Samuel Oschin Telescope 48 inch and the 60 inch Telescope at the Palomar Observatory as part of the Zwicky Transient Facility project. ZTF is supported by the National Science Foundation under grant No. AST-1440341 and a collaboration including Caltech, IPAC, the Weizmann Institute of Science, the Oskar Klein Center at Stockholm University, the University of Maryland, the University of Washington, Deutsches Elektronen-Synchrotron and Humboldt University, Los Alamos National Laboratories, the TANGO Consortium of Taiwan, the University of Wisconsin at Milwaukee, and Lawrence Berkeley National Laboratories. Operations are conducted by COO, IPAC, and UW. SED Machine is based upon work supported by the National Science Foundation under grant No. 1106171.

This work is also based on observations made with the Nordic Optical Telescope, owned in collaboration by the University of Turku and Aarhus University, and operated jointly by Aarhus University, the University of Turku and the University of Oslo, representing Denmark, Finland and

Norway, the University of Iceland and Stockholm University at the Observatorio del Roque de los Muchachos, La Palma, Spain, of the Instituto de Astrofisica de Canarias.

A major upgrade of the Kast spectrograph on the Shane 3 m telescope at Lick Observatory, led by Brad Holden, was made possible through gifts from the Heising-Simons Foundation, William and Marina Kast, and the University of California Observatories. Research at Lick Observatory is partially supported by a generous gift from Google. The W. M. Keck Observatory is operated as a scientific partnership among the California Institute of Technology, the University of California and NASA; the observatory was made possible by the generous financial support of the W. M. Keck Foundation. W. M. Keck Observatory access was supported by Northwestern University and the Center for Interdisciplinary Exploration and Research in Astrophysics (CIERA).

Facilities: PO:1.2 m (ZTF), PO:1.5 m (SEDM), Gemini: Gillett (GNIRS), Hale (DBSP), NOT (ALFOSC), Shane (Kast Double spectrograph), Keck:I (LRIS), Keck:II (DEIMOS).

Software: astropy (Astropy Collaboration et al. 2013, 2018), CASTRO (Almgren et al. 2010), dynesty (Speagle 2020), emcee (Foreman-Mackey et al. 2013), LAMBDAR (Wright 2016), matplotlib (Hunter 2007), prospector (Johnson et al. 2021), PypeIt (Prochaska et al. 2020), pysedm (Rigault et al. 2019), Python-FSPS (Conroy et al. 2009; Conroy & Gunn 2010), scipy (Virtanen et al. 2020), seaborn (Waskom 2021), SEDONA (Kasen et al. 2006).

Appendix Comparison to DDet Models with Various Shell Masses

We have shown that the $r_{\rm ZTF}$ -band light curve and the observed spectra of SN 2020jgb near maximum brightness are fairly consistent with the DDet of a sub- $M_{\rm Ch}$ WD beneath a massive shell ($\sim 0.13\,M_{\odot}$), whose total mass is $\sim 0.95-1.00\,M_{\odot}$. In this appendix we compare SN 2020jgb to other DDet models developed using the methods in Polin et al. (2019).

Figure 9 shows multiple models with a total mass of $\sim 0.95\,M_\odot$, all of which reproduce the brightness of SN 2020jgb in $r_{\rm ZTF}$ if there is no host extinction. The $g_{\rm ZTF}$ -band synthetic light curves, which depend on the strength of line-blanketing of the Fe-group elements, differ significantly depending on the He-shell mass. In the two models with thinner shells ($\lesssim 0.08\,M_\odot$), the suppression of flux blueward of $\sim 5000\,\text{Å}$ is much less significant than that seen in SN 2020jgb at $-4\,$ days. As a result, they overestimate the brightness in $g_{\rm ZTF}$ before maximum light. The $0.84\,M_\odot + 0.11\,M_\odot$ model shows the most significant line-blanketing.

Figure 10 shows models with a total mass of $\sim 1.00\,M_\odot$ assuming $E(B-V)_{\rm host}=0.13$ mag. Each model reproduces the brightness of SN 2020jgb in $r_{\rm ZTF}$. The model with the thinnest shell significantly underestimates the level of line-blanketing, allowing us to eliminate it as a viable model for SN 2020jgb. Models with shells $\gtrsim 0.05\,M_\odot$ exhibit similar behavior, meaning the shell mass is quite uncertain. We note that all the $1.00\,M_\odot$ models overestimate the maximum brightness of SN 2020jgb in $g_{\rm ZTF}$ and underestimate the level of line-blanketing in the spectrum at -4 days.

While none of the models presented here provides a perfect match to the observations, SN 2020jgb is more consistent with

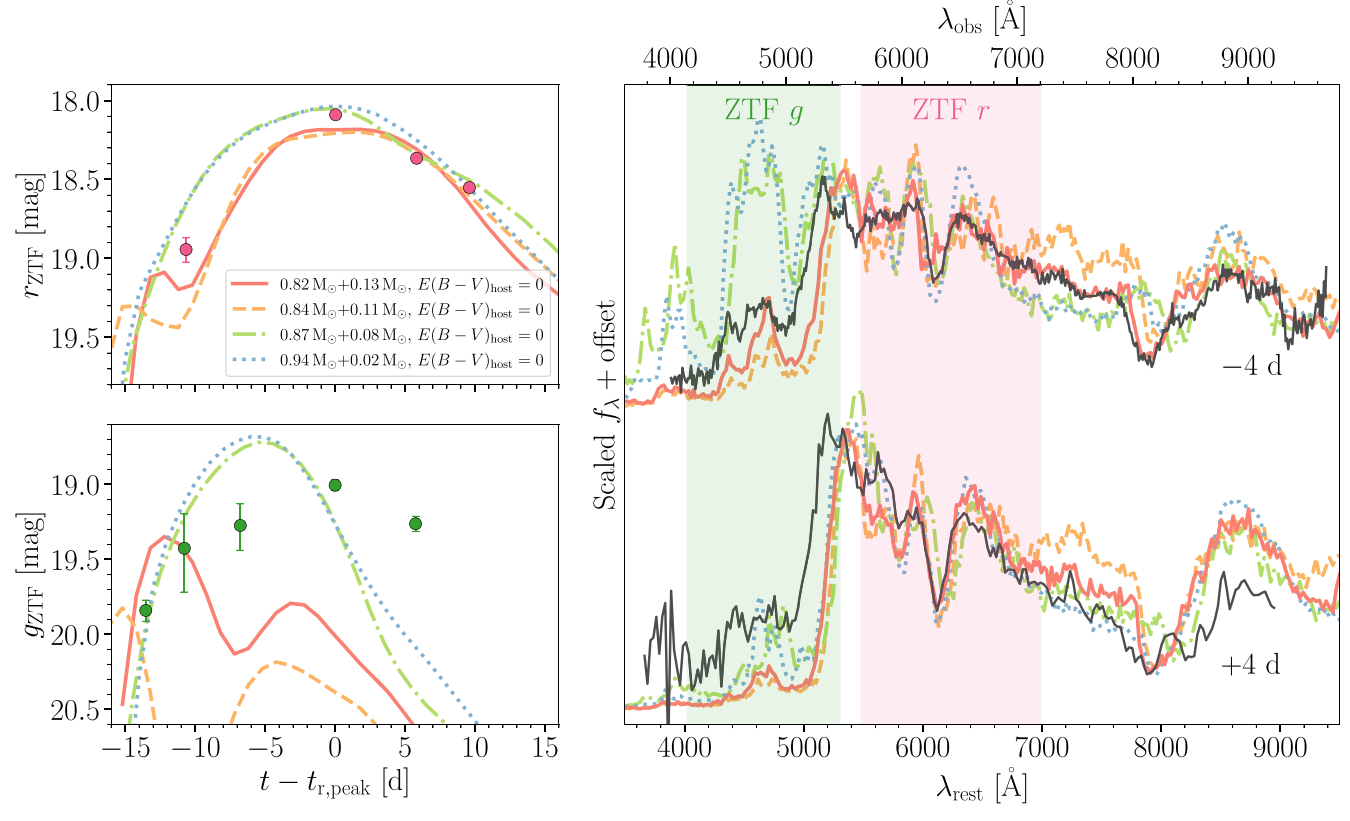


Figure 9. Similar to Figure 4, but more models with a total mass of $\sim 0.95 \, M_\odot$ and various shell masses (from 0.02 to 0.13 M_\odot) are displayed. For these models, we assume no host extinction.

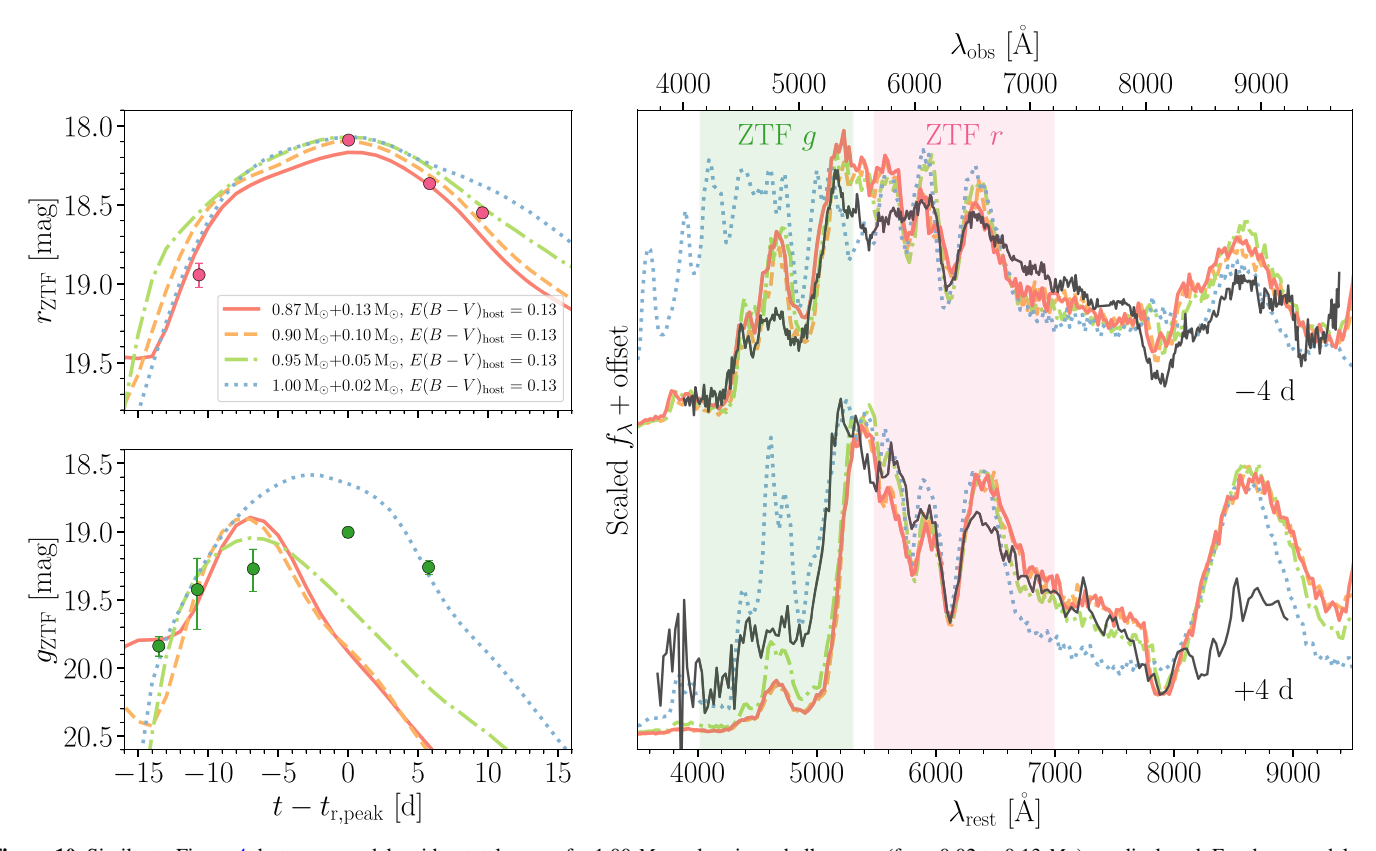


Figure 10. Similar to Figure 4, but more models with a total mass of $\sim 1.00~M_{\odot}$ and various shell masses (from 0.02 to 0.13 M_{\odot}) are displayed. For these models, we assume $E(B-V)_{\rm host}=0.13$.

He-shell DDet models with relatively massive ($\gtrsim 0.1\,M_{\odot}$) shells.

ORCID iDs Chang Liu (刘畅) ® https://orcid.org/0000-0002-7866-4531

Adam A. Miller https://orcid.org/0000-0001-9515-478X Abigail Polin https://orcid.org/0000-0002-1633-6495 Anya E. Nugent https://orcid.org/0000-0002-2028-9329 Kishalay De https://orcid.org/0000-0002-8989-0542 Peter E. Nugent https://orcid.org/0000-0002-3389-0586 Steve Schulze https://orcid.org/0000-0001-6797-1889 Avishay Gal-Yam https://orcid.org/0000-0002-3653-5598 Christoffer Fremling https://orcid.org/0000-0002-4223-103X Shreya Anand https://orcid.org/0000-0003-3768-7515 Igor Andreoni https://orcid.org/0000-0002-8977-1498 Peter Blanchard https://orcid.org/0000-0003-0526-2248 Thomas G. Brink https://orcid.org/0000-0001-5955-2502 Suhail Dhawan https://orcid.org/0000-0002-2376-6979 Alexei V. Filippenko https://orcid.org/0000-0003-3460-0103 Kate Maguire https://orcid.org/0000-0002-9770-3508 Tassilo Schweyer https://orcid.org/0000-0001-8948-3456 Huei Sears https://orcid.org/0000-0001-8023-4912 Yashvi Sharma https://orcid.org/0000-0003-4531-1745 Matthew J. Graham https://orcid.org/0000-0002-3168-0139 Steven L. Groom https://orcid.org/0000-0001-5668-3507 Mansi M. Kasliwal https://orcid.org/0000-0002-5619-4938 Frank J. Masci https://orcid.org/0000-0002-8532-9395 Josiah Purdum https://orcid.org/0000-0003-1227-3738 Benjamin Racine https://orcid.org/0000-0001-8861-3052 Jesper Sollerman https://orcid.org/0000-0003-1546-6615 Shrinivas R. Kulkarni https://orcid.org/0000-0001-5390-8563

```
References
Ahn, C. P., Alexandroff, R., Allende Prieto, C., et al. 2012, ApJS, 203, 21
Almgren, A. S., Beckner, V. E., Bell, J. B., et al. 2010, ApJ, 715, 1221
Ashall, C., Lu, J., Shappee, B. J., et al. 2022, ApJL, 932, L2
Astropy Collaboration, Price-Whelan, A. M., Sipőcz, B. M., et al. 2018, AJ,
   156, 123
Astropy Collaboration, Robitaille, T. P., Tollerud, E. J., et al. 2013, A&A,
   558, A33
Baldwin, J. A., Phillips, M. M., & Terlevich, R. 1981, PASP, 93, 5
Bellm, E. C., Kulkarni, S. R., Barlow, T., et al. 2019b, PASP, 131, 068003
Bellm, E. C., Kulkarni, S. R., Graham, M. J., et al. 2019a, PASP, 131, 018002
Blagorodnova, N., Neill, J. D., Walters, R., et al. 2018, PASP, 130, 035003
Blondin, S., & Tonry, J. L. 2007, ApJ, 666, 1024
Boyle, A., Sim, S. A., Hachinger, S., & Kerzendorf, W. 2017, A&A, 599, A46
Brinchmann, J., Charlot, S., White, S. D. M., et al. 2004, MNRAS, 351, 1151
Bulla, M., Miller, A. A., Yao, Y., et al. 2020, ApJ, 902, 48
Byler, N., Dalcanton, J. J., Conroy, C., & Johnson, B. D. 2017, ApJ, 840, 44
Cao, Y., Kulkarni, S. R., Howell, D. A., et al. 2015, Natur, 521, 328
Cardelli, J. A., Clayton, G. C., & Mathis, J. S. 1989, ApJ, 345, 245
Carrick, J., Turnbull, S. J., Lavaux, G., & Hudson, M. J. 2015, MNRAS,
   450, 317
Cenko, S. B., Fox, D., Moon, D.-S., et al. 2006, PASP, 118, 1396
Chabrier, G. 2003, PASP, 115, 763
Chambers, K. C., Magnier, E. A., Metcalfe, N., et al. 2016, arXiv:1612.05560
Childress, M. J., Filippenko, A. V., Ganeshalingam, M., & Schmidt, B. P.
   2014, MNRAS, 437, 338
Childress, M. J., Scalzo, R. A., Sim, S. A., et al. 2013, ApJ, 770, 29
Conroy, C., & Gunn, J. E. 2010, ApJ, 712, 833
Conroy, C., Gunn, J. E., & White, M. 2009, ApJ, 699, 486
Cook, D. O., Kasliwal, M. M., Sistine, A. V., et al. 2019, ApJ, 880, 7
Dahiwale, A., & Fremling, C. 2020, TNSCR, 2020-1624, 1
```

```
De, K., Kasliwal, M. M., Polin, A., et al. 2019, ApJL, 873, L18
De, K., Kasliwal, M. M., Tzanidakis, A., et al. 2020, ApJ, 905, 58
de los Reyes, M. A. C., Kirby, E. N., Seitenzahl, I. R., & Shen, K. J. 2020, ApJ,
Deckers, M., Maguire, K., Magee, M. R., et al. 2022, MNRAS, 512, 1317
Dekany, R., Smith, R. M., Riddle, R., et al. 2020, PASP, 132, 038001
Dessart, L., & Hillier, D. J. 2015, MNRAS, 447, 1370
Dey, A., Schlegel, D. J., Lang, D., et al. 2019, AJ, 157, 168
Dimitriadis, G., Foley, R. J., Rest, A., et al. 2019, ApJL, 870, L1
Dong, Y., Milisavljevic, D., Leja, J., et al. 2022b, ApJ, 927, 199
Dong, Y., Valenti, S., Polin, A., et al. 2022a, ApJ, 934, 102
Duev, D. A., Mahabal, A., Masci, F. J., et al. 2019, MNRAS, 489, 3582
Eitner, P., Bergemann, M., Ruiter, A. J., et al. 2022, arXiv:2206.10258
Elias, J. H., Fowler, A. M., Vukobratovich, D., et al. 1998, Proc. SPIE,
   3354, 555
Faber, S. M., Phillips, A. C., Kibrick, R. I., et al. 2003, Proc. SPIE, 4841, 1657
Filippenko, A. V., Chornock, R., Swift, B., et al. 2003, IAU Circ., 8159, 2
Filippenko, A. V., Richmond, M. W., Branch, D., et al. 1992, AJ, 104, 1543
Fink, M., Röpke, F. K., Hillebrandt, W., et al. 2010, A&A, 514, A53
Fitzpatrick, E. 1999, PASP, 111, 63
Foley, R. J. 2015, MNRAS, 452, 2463
Foley, R. J., Challis, P. J., Chornock, R., et al. 2013, ApJ, 767, 57
Foreman-Mackey, D., Hogg, D. W., Lang, D., & Goodman, J. 2013, PASP,
Fremling, C. 2020, TNSTR, 2020-1247, 1
Galbany, L., Ashall, C., Hoflich, P., et al. 2019, A&A, 630, A76
Gallazzi, A., Charlot, S., Brinchmann, J., White, S. D. M., & Tremonti, C. A.
   2005, MNRAS, 362, 41
Gal-Yam, A. 2017, in Handbook of Supernovae, ed. A. W. Alsabti &
  P. Murdin (Cham: Springer), 195
Ganeshalingam, M., Li, W., Filippenko, A. V., et al. 2012, ApJ, 751, 142
Geier, S., Marsh, T. R., Wang, B., et al. 2013, A&A, 554, A54
Graham, M. J., Kulkarni, S. R., Bellm, E. C., et al. 2019, PASP, 131, 078001
Gronow, S., Collins, C., Ohlmann, S. T., et al. 2020, A&A, 635, A169
Höflich, P., Gerardy, C. L., Fesen, R. A., & Sakai, S. 2002, ApJ, 568, 791
Hosseinzadeh, G., Sand, D. J., Lundqvist, P., et al. 2022, ApJL, 933, L45
Hosseinzadeh, G., Sand, D. J., Valenti, S., et al. 2017, ApJL, 845, L11
Hsiao, E. Y., Burns, C. R., Contreras, C., et al. 2015, A&A, 578, A9
Hsiao, E. Y., Phillips, M. M., Marion, G. H., et al. 2019, PASP, 131, 014002
Hunter, J. D. 2007, CSE, 9, 90
Iben, I., Jr., Nomoto, K., Tornambe, A., & Tutukov, A. V. 1987, ApJ, 317, 717
Inserra, C., Sim, S. A., Wyrzykowski, L., et al. 2015, ApJL, 799, L2
Jacobson-Galán, W. V., Polin, A., Foley, R. J., et al. 2020, ApJ, 896, 165
Jerkstrand, A. 2017, in Handbook of Supernovae, ed. A. W. Alsabti &
  P. Murdin (Cham: Springer), 795
Jha, S. W., Maguire, K., & Sullivan, M. 2019, NatAs, 3, 706
Jiang, J.-a., Doi, M., Maeda, K., et al. 2017, Natur, 550, 80
Jiang, J.-a., Maeda, K., Kawabata, M., et al. 2021, ApJL, 923, L8
Johnson, B. D., Leja, J., Conroy, C., & Speagle, J. S. 2021, ApJS, 254, 22
Kasen, D., Thomas, R. C., & Nugent, P. 2006, ApJ, 651, 366
Kasliwal, M. M., Cannella, C., Bagdasaryan, A., et al. 2019, PASP, 131, 038003
Kasliwal, M. M., Kulkarni, S. R., Gal-Yam, A., et al. 2012, ApJ, 755, 161
Kauffmann, G., Heckman, T. M., Simon White, D. M., et al. 2003, MNRAS,
   341, 33
Kromer, M., Sim, S. A., Fink, M., et al. 2010, ApJ, 719, 1067
Kupfer, T., Bauer, E. B., van Roestel, J., et al. 2022, ApJL, 925, L12
Lang, D. 2014, AJ, 147, 108
Leroy, A. K., Sandstrom, K. M., Lang, D., et al. 2019, ApJS, 244, 24
Li, W., Filippenko, A., Chornock, R., et al. 2003, PASP, 115, 453
Livne, E. 1990, ApJL, 354, L53
Livne, E., & Arnett, D. 1995, ApJ, 452, 62
Lucy, L. B. 1991, ApJ, 383, 308
Lunnan, R., Kasliwal, M. M., Cao, Y., et al. 2017, ApJ, 836, 60
Lyman, J. D., Levan, A. J., Church, R. P., Davies, M. B., & Tanvir, N. R. 2014,
          S, 444, 2157
Magee, M. R., Maguire, K., Kotak, R., & Sim, S. A. 2021, MNRAS, 502, 3533
Maguire, K., Sullivan, M., Pan, Y. C., et al. 2014, MNRAS, 444, 3258
Mahabal, A., Rebbapragada, U., Walters, R., et al. 2019, PASP, 131, 038002
Mainzer, A., Bauer, J., Cutri, R. M., et al. 2014, ApJ, 792, 30
Maoz, D., Mannucci, F., & Nelemans, G. 2014, ARA&A, 52, 107
Marion, G. H., Brown, P. J., Vinkó, J., et al. 2016, ApJ, 820, 92
Marion, G. H., Höflich, P., Gerardy, C. L., et al. 2009, AJ, 138, 727
Martin, D. C., Fanson, J., Schiminovich, D., et al. 2005, ApJL, 619, L1
Masci, F. J., Laher, R. R., Rusholme, B., et al. 2019, PASP, 131, 018003
Matheson, T., Filippenko, A. V., Barth, A. J., et al. 2000, AJ, 120, 1487
Mazzali, P. A., Benetti, S., Altavilla, G., et al. 2005, ApJL, 623, L37
```

```
Mazzali, P. A., Sullivan, M., Filippenko, A. V., et al. 2015, MNRAS,
   450, 2631
Mazzali, P. A., Sullivan, M., Hachinger, S., et al. 2014, MNRAS, 439, 1959
McMahon, R. G., Banerji, M., Gonzalez, E., et al. 2013, Msngr, 154, 35
Meisner, A. M., Lang, D., & Schlegel, D. J. 2017a, AJ, 153, 38
Meisner, A. M., Lang, D., & Schlegel, D. J. 2017b, AJ, 154, 161
Miller, A. A., Kasliwal, M. M., Cao, Y., et al. 2017, ApJ, 848, 59
Miller, A. A., Magee, M. R., Polin, A., et al. 2020, ApJ, 898, 56
Miller, J., & Stone, R. 1994, The Kast Double Spectograph, Lick Observatory
   Technical rep., 66 University of California Observatories/Lick Observatory
Ni, Y. Q., Moon, D.-S., Drout, M. R., et al. 2022, NatAs, 6, 568
Ni, Y. Q., Moon, D.-S., Drout, M. R., et al. 2023, ApJ, 946, 7
Nomoto, K. 1982a, ApJ, 253, 798
Nomoto, K. 1982b, ApJ, 257, 780
Nugent, A. E., Fong, W., Dong, Y., et al. 2020, ApJ, 904, 52
Nugent, A. E., Fong, W., Dong, Y., et al. 2022, ApJ, 940, 57
Oke, J. B., Cohen, J. G., Carr, M., et al. 1995, PASP, 107, 375
Oke, J. B., & Gunn, J. E. 1982, PASP, 94, 586
Osterbrock, D. E., & Ferland, G. J. 2006, Astrophysics of Gaseous Nebulae
   and Active Galactic Nuclei (Sausalito, CA: University Science Books)
Patterson, M. T., Bellm, E. C., Rusholme, B., et al. 2019, PASP, 131, 018001
Pereira, R., Thomas, R. C., Aldering, G., et al. 2013, A&A, 554, A27
Perets, H. B., Gal-Yam, A., Mazzali, P. A., et al. 2010, Natur, 465, 322
Polin, A., Nugent, P., & Kasen, D. 2019, ApJ, 873, 84
Polin, A., Nugent, P., & Kasen, D. 2021, ApJ, 906, 65
Poznanski, D., Ganeshalingam, M., Silverman, J. M., & Filippenko, A. V.
   2011, MNRAS, 415, L81
Prochaska, J., Hennawi, J., Westfall, K., et al. 2020, JOSS, 5, 2308
Prochaska, J. X., Hennawi, J., Cooke, R., et al. 2020, pypeit/PypeIt: Release
   v1.0.0, Zenodo, doi:10.5281/zenodo.3743493
Rigault, M., Neill, J. D., Blagorodnova, N., et al. 2019, A&A, 627, A115
Sanders, J. L., Belokurov, V., & Man, K. T. F. 2021, MNRAS, 506, 4321
```

Schlafly, E. F., & Finkbeiner, D. P. 2011, ApJ, 737, 103

```
Schulze, S., Yaron, O., Sollerman, J., et al. 2021, ApJS, 255, 29
Shahbandeh, M., Hsiao, E. Y., Ashall, C., et al. 2022, ApJ, 925, 175
Shen, K. J., Boos, S. J., Townsley, D. M., & Kasen, D. 2021, ApJ, 922, 68
Shen, K. J., & Moore, K. 2014, ApJ, 797, 46
Shen, K. J., Quataert, E., & Pakmor, R. 2019, ApJ, 887, 180
Silverman, J. M., Foley, R. J., Filippenko, A. V., et al. 2012, MNRAS,
  425, 1789
Silverman, J. M., Vinkó, J., Marion, G. H., et al. 2015, MNRAS, 451, 1973
Sim, S. A., Fink, M., Kromer, M., et al. 2012, MNRAS, 420, 3003
Skrutskie, M. F., Cutri, R. M., Stiening, R., et al. 2003, 2MASS All-Sky Point
  Source Catalog, IPAC, doi:10.26131/IRSA2
Skrutskie, M. F., Cutri, R. M., Stiening, R., et al. 2006, AJ, 131, 1163
Smith, M., Nichol, R. C., Dilday, B., et al. 2012, ApJ, 755, 61
Speagle, J. S. 2020, MNRAS, 493, 3132
Sullivan, M., Le Borgne, D., Pritchet, C. J., et al. 2006, ApJ, 648, 868
Sun, F., & Gal-Yam, A. 2017, arXiv:1707.02543
Townsley, D. M., Miles, B. J., Shen, K. J., & Kasen, D. 2019, ApJL, 878, L38
UnWISE Team 2021, unWISE Images, IPAC, doi:10.26131/IRSA524
Valenti, S., Yuan, F., Taubenberger, S., et al. 2014, MNRAS, 437, 1519
Veilleux, S., & Osterbrock, D. E. 1987, ApJS, 63, 295
Virtanen, P., Gommers, R., Oliphant, T. E., et al. 2020, NatMe, 17, 261
Waskom, M. 2021, JOSS, 6, 3021
Woosley, S. E., & Kasen, D. 2011, ApJ, 734, 38
Woosley, S. E., Taam, R. E., & Weaver, T. A. 1986, ApJ, 301, 601
Woosley, S. E., & Weaver, T. A. 1994, ApJ, 423, 371
Wright, A. H. 2016, LAMBDAR: Lambda Adaptive Multi-Band Deblending
   Algorithm in R, Astrophysics Source Code Library, record ascl:1604.003
Wright, E. L., Eisenhardt, P. R. M., Mainzer, A. K., et al. 2010, AJ, 140,
Yao, Y., Miller, A. A., Kulkarni, S. R., et al. 2019, ApJ, 886, 152
Yaron, O., & Gal-Yam, A. 2012, PASP, 124, 668
York, D. G., Adelman, J., Anderson, J. E., Jr., et al. 2000, AJ, 120, 1579
Zackay, B., Ofek, E. O., & Gal-Yam, A. 2016, ApJ, 830, 27
```